Physical Processes Leading to Extreme Day-to-Day Temperature Change, Part I: Present-day Climate

Kalpana Hamal and Stephan Pfahl

5   Institut für Meteorologie, Freie Universität Berlin, 12165 Berlin., Germany

Correspondence to: Kalpana Hamal (_k.hamal@fu-berlin.de_)

Abstract

Extreme temperature changes from one day to another, either associated with warming or cooling, can have a significant impact on health, the environment, and society. Previous studies have quantified that such day-to-day temperature (DTDT)

10   changes are typically more pronounced in the extratropics than the tropics. However, the underlying physical processes and the relationship between extreme events and the large-scale atmospheric circulation remain poorly understood. Here, these processes are investigated for different locations around the globe based on ERA5 reanalysis data and Lagrangian backward trajectory calculations. We show that extreme DTDT changes in the extratropics are generally associated with changes in air mass transport, particularly shifts from warmer to colder air parcels or vice versa, linked to regionally specific synoptic-scale

15   circulation anomalies (ridge or trough patterns). These dominant effects of advection are modulated by changes in adiabatic and diabatic processes in the transported air parcels, which either amplify or dampen DTDT decreases (cooling events) and increases (warming events) depending on the region and season. In contrast, extreme DTDT changes during December-February in the tropics are controlled by local processes rather than changes in advection. For instance, the most significant DTDT decreases are associated with a shift from less cloudy to more cloudy conditions, highlighting the crucial role of solar

20   radiative heating. The mechanistic insights into extreme DTDT changes obtained in this study can help improve the prediction of such events and anticipate future changes in their occurrence frequency and intensity, which will be investigated in part II of this study.

1. Introduction

Day-to-day temperature (DTDT) changes, here represented by temperature differences between consecutive days, can have

25   significant implications across various sectors, including economic, ecology, and human health (Gough, 2008; Zhou et al., 2020; Kotz et al., 2021; Hovdahl, 2022). A change in DTDT variation is linked to increased mortality rates, with the impact varying across geographic regions such as northern latitudes, tropics, and southern latitudes (Chan et al., 2012; Hovdahl, 2022; Sarmiento, 2023; Wu et al., 2022a). A recent study further reveals that temperature changes can impact heat-related mortality by regionally up to more than 7% of total deaths (Wu et al., 2022b). High DTDT variation has a negative effect on

30   economic activity (Linsenmeier, 2023), with economic losses exhibiting regional disparities, as a 1°C increase in DTDT

change results in an increase of 3-5% in vulnerability in mid and high-latitude areas but more than 10% in low-latitude and coastal regions (Kotz et al., 2021). These previous studies highlight the critical need for comprehensive studies investigating DTDT variation and the underlying atmospheric processes in the present climate.

35 With regard to long-term trends in DTDT change, the early study by Karl et al. (1995) observed a decrease at mid-to-high latitude stations, particularly during the summer season, while no significant trend was detected in Australia. Recently, Xu et al. (2020) extended these results by demonstrating a substantial increase in summer DTDT change across diverse regions such as the Arctic coast, South China, and Australia, but decreasing winter DTDT change in mid to high latitudes. These trends align with the comprehensive analysis by Krauskopf and Huth (2024) and Wan et al. (2021), attributing

40 spatiotemporal fluctuations in global temperature variability, except during boreal summer, to anthropogenic influences. Although most prior investigations have predominantly focused on analyzing trends in the average magnitude of DTDT change, it is equally important to understand extreme DTDT changes. The concept of extreme DTDT events, characterized by daily average temperature changes larger than ±10°C, has been introduced in a recent study that only focused on mid-high latitudes (Zhou et al., 2020). Since higher DTDT variation is observed in the northern mid-high latitudes, spanning regions

45 such as North Asia, the United States, and Europe (Gough, 2008; Xu et al., 2020), we can also expect more pronounced extreme DTDT changes in these regions compared to lower latitudes (Figures 2a-d), which is consistent with the findings of Zhou et al. (2020). Here, to account for such regional differences and investigate extreme DTDT changes globally, we utilize percentile-based thresholds, as widely used for identifying temperature extremes (Bieli et al., 2015; Pfahl, 2014; Nygård et al., 2023).

50

The relationship between daily temperature extremes (extremely high or low temperature, not extreme DTDT changes) and distinct circulation patterns at global and regional scales has been thoroughly investigated (Horton et al., 2015; Adams et al., 2021; Nygård et al., 2023; Pfahl, 2014). For example, in Europe, extreme warm events in summer often coincide with blocking anticyclones or subtropical ridges, while winter cold extremes are linked to North Atlantic blocking, facilitating the

55 intrusion of cold air masses (Nygård et al., 2023; Kautz et al., 2022; Pfahl and Wernli, 2012; Sillmann et al., 2011). Similarly, warm extremes in North America correlate with anticyclonic circulation and ridges, whereas extreme cold is linked to troughs and advection of continental air masses (Adams et al., 2021; Wang et al., 2019). Key drivers of DTDT variability are frontal structures (Ghil and Lucarini, 2020), and the relevance of fronts for European DTDT extremes has been confirmed in the detailed study by Piskala and Huth (2020). Further, particular insights into the physical processes

60 associated with daily temperature extremes have been obtained from Lagrangian studies based on air parcel trajectory analyses, which have quantified the contributions of advection, adiabatic, and diabatic heating/cooling to temperature extremes (Schumacher et al., 2019; Bieli et al., 2015; Röthlisberger and Papritz, 2023b, a; Zschenderlein et al., 2019; Hartig et al., 2023). All these studies highlight the significance of specific circulation anomalies for causing extreme weather in mid-to-high latitudes. In contrast, tropical regions generally experience much weaker temperature advection compared to the

extratropics, and extreme temperature events there are more strongly influenced by local processes such as precipitation, radiation, cloud cover, and surface fluxes (Gough, 2008; Matuszko et al., 2004; Sun and Mahrt, 1995; Dirmeyer et al., 2022). Nevertheless, an accelerated warming of extreme temperatures across tropical land has been observed recently (Byrne, 2021). These previous studies have established the groundwork for understanding the origins of daily temperature extremes, providing a fundamental basis also for deeper investigations into extreme DTDT changes globally.

This paper investigates in detail the influence of altering air mass properties within the large-scale atmospheric circulation on extreme DTDT changes. We use observations and reanalysis data to quantify the magnitude of extreme DTDT changes worldwide. To study the underlying processes, we apply a composite approach and perform a Lagrangian analysis, calculating backward trajectories of surface air masses from selected locations on the two days involved in extreme DTDT changes. The contributions of temperature advection, adiabatic, and diabatic processes are then quantified following previous studies of temperature extremes (Bieli et al., 2015; Röthlisberger and Papritz, 2023a; Santos et al., 2015; Röthlisberger and Papritz, 2023b; Nygård et al., 2023). We aim to address the following research questions: (1) Which (changes in) atmospheric circulation patterns occur on consecutive days associated with extreme DTDT changes? (2) Which physical processes contribute to the occurrences of extreme DTDT changes?

2. Data and Method

2.1 ERA5

ERA5 is the fifth-generation European Centre for Medium-Range Weather Forecasts (ECMWF) global reanalysis product, providing climate and weather data for the past eight decades. It was developed by 4D-Var data assimilation in cycle CY41R2 of the ECMWF Integrated Forecasting System (Hersbach et al., 2020). It is an updated version of the widely used ERA-Interim reanalysis, employing a newer version of the ECMWF Earth system model with 137 hybrid sigma/pressure levels in the vertical up to 0.01 hPa (Hersbach, 2019). It provides hourly estimates of several atmospheric, ocean-wave, and land-surface quantities on a regular latitude-longitude grid of 0.25 degrees. Recently, ERA5 data has been used for different climate and weather-related global and regional studies (Böker et al., 2023; Simmons, 2022), and some have recommended it as the best alternative for regions with sparse observational coverage (Sharma et al., 2020; Sheridan et al., 2020). We use ERA5 data from 1980 to 2020, encompassing global daily mean 2m-surface air temperature (calculated from hourly temperature), total precipitation, and several three-dimensional atmospheric fields (temperature, horizontal and vertical winds, geopotential). The spatial resolution for all analyses is $0.25° \times 0.25°$, except for the trajectory calculations, for which input data at a horizontal resolution of $0.5° \times 0.5°$ are employed. The temporal resolution of the near-surface temperature and composite analysis is daily, while the input data for the trajectories has an hourly resolution. We have compared the magnitude of DTDT changes from ERA5 data with observational datasets (HadGHCND and Berkeley Earth Surface Temperatures (BEST)), with a detailed description of the datasets available in the supplementary material.

2.2 DTDT variation and extremes

This study defines DTDT change, denoted as δ_T, as the difference in daily mean near-surface air temperature between the previous day (T_{t-1}) and the day of the event (T_t), as shown in Eq. (1).

$$\delta_T = (T_t - T_{t-1})   \tag{1}$$

The average daily temperature change, μ_{DTDT} reflects the difference between the temperatures at the start (T_0) and end (T_n) of the time series (Eq. 2).

$$\mu_{DTDT} = \frac{1}{n} \sum_{t=1}^{n}(T_t - T_{t-1}) = T_n - T_0   \tag{2}$$

To capture typical DTDT changes, we thus use the standard deviation, σ_{DTDT}, as shown in Eq. (3).

$$\sigma_{DTDT}^2 = \frac{1}{n} \sum_{t=1}^{n}(T_t - T_{t-1})^2   \tag{3}$$

By inserting the average daily temperature μ_T and multiplying out the square bracket, we find a relationship between σ_{DTDT}, the standard deviation of the daily mean temperature (σ_T) and the covariance between consecutive days (COV (T_t, T_{t-1})):

$$\sigma_{DTDT}^2 = \frac{1}{n} \sum_{t=1}^{n}((T_t - \mu_T) - (T_{t-1} - \mu_T))^2$$

$$= \frac{1}{n} \sum_{t=1}^{n}((T_t - \mu_T)^2 + (T_{t-1} - \mu_T)^2 - 2(T_t - \mu_T)(T_{t-1} - \mu_T)$$

$$\approx 2\sigma_T^2 - 2COV(T_t, T_{t-1})   \tag{4}$$

The approximation in equation (4) is based on the fact that, for large n, both $\frac{1}{n} \sum_{t=1}^{n}(T_{t-1} - \mu_T))^2$ and $\frac{1}{n} \sum_{t=1}^{n}(T_t - \mu_T))^2$ are good estimators of σ_T^2. Finally, the standard deviation of DTDT can thus be expressed as a function of the usual standard deviation (σ_T) and the lag-1 autocorrelation ($r_{1,T}$) of daily mean temperature, as shown in Eq. (5).

$$\sigma_{DTDT} = \sigma_T \sqrt{2(1-r_{1,T})}   \tag{5}$$

In addition, extreme DTDT changes are studied using the percentile method. Extreme cooling and warming events at each grid box are identified using the 5th and 95th percentiles of the DTDT change distribution as thresholds, respectively. The analyses focus on the two main seasons: December-February (DJF) and July-August (JJA). Accordingly, 184 events in DJF and 188 events in JJA are selected at each location based on the ERA5 dataset.

2.3 Trajectory setup

The Lagrangian analysis tool (LAGRANTO), introduced by Sprenger and Wernli (2015), is used to calculate backward trajectories of near-surface air masses on days associated with extreme DTDT changes from 1980 to 2020. The trajectories are initialized at 18 UTC on both the preceding day (t-1) and on the event day (t) at 10, 30, 50, and 100 hPa above the surface at the corresponding grid cells. Similar to studies on extreme temperatures (Zschenderlein et al., 2019), the different initialization heights are used to sample a near-surface layer that is assumed to be well-mixed. The time difference of 24

hours between the two initializations allows for a proper separation of the air masses before and after the temperature change. Although LAGRANTO is used to calculate 10-day backward trajectories, extremes typically develop on a timescale of 2–3 day (Bieli et al., 2015; Röthlisberger and Papritz, 2023a). Therefore, we focus on 3-day backward trajectories for the analysis. Various variables of interest, including latitude, longitude, pressure, temperature, and potential temperature, are
130   interpolated along the trajectory paths and saved at 1-hour intervals.

2.4 Lagrangian temperature variability decomposition

To better understand the underlying mechanisms of extreme DTDT changes, our analysis focuses on four specific locations: two grid boxes in the Northern Hemisphere mid-latitudes: North America (52°N, 86°W) and Europe (50°N, 10°E)), one in tropical South America (13°S, 24°E), and another on the southern coast of Australia (37°S, 140°E). The results for a few
135   additional grid boxes (Northern Asia (70°N, 90°E), Southern South America (37°S, 68°W), South Asia (23°N, 80°E), South Africa (13°S, 24°E), and Western North America (45°N, 120°W)) are presented in the supplementary material. At these locations, we introduce a novel Lagrangian temperature variability decomposition method to quantify contributions of advection, adiabatic, and diabatic processes to extreme DTDT changes, similar to approaches used for near-surface hot and cold extremes (Röthlisberger and Papritz, 2023b, a). This decomposition is applied to backward trajectories initiated on the
140   two days (t-1 and t) involved in extreme DTDT changes, focusing on a 3-day Lagrangian time scale. The appendix presents a detailed derivation of the diagnostic, leading to the decomposition given in Eq. (6).

$$\delta_T^0 \approx \delta_{\overline{T}}^{-3d} + \delta_{\overline{T}}^{adi} + \delta_{\overline{T}}^{dia} + res \qquad (6)$$

145   The DTDT change at the surface (δ_T^0) is decomposed into three contributing factors: the mean temperature difference at the origin of the air parcels, three days before initialization, indicates the contribution of advection ($\delta_{\overline{T}}^{-3d}$). When the original temperature of the air parcels initialized on the previous day ($\overline{T}_{t-1}^{-3d}$) is higher than the original temperature of the air parcels initialized at the event ($\overline{T}_t^{-3d}$), this represents a shift from the advection of originally warmer air on the preceding day to colder air on the event day, which is referred to as cold air advection. The reverse is true for warm air advection. Further
150   contributions come from mean adiabatic warming or cooling resulting from vertical descent or ascent, respectively ($\delta_{\overline{T}}^{adi}$), and mean diabatic heating or cooling from processes such as latent heating in clouds, radiation, and surface fluxes ($\delta_{\overline{T}}^{dia}$). Furthermore, the final term is the residuum (res), resulting from numerical inaccuracies in the calculation of derivatives. The residual is typically small and is thus not further discussed in the following text and the figures.

3. Result

3.1 DTDT variations in DJF and JJA

Both the ERA5 and Observations (HadGHCND and BEST) datasets reveal that the magnitude of DTDT variations, quantified by σ_{DTDT} is larger in the extratropics than in the tropics during DJF and JJA (Figures 1a-b and S1a-d). Notably, σ_{DTDT} is larger during DJF than in JJA in the Northern Hemisphere, while the seasonal cycle is less clear in the Southern Hemisphere, with higher σ_{DTDT} in JJA in Antarctica, central South America, South Africa, and northern Australia, but higher σ_{DTDT} in DJF in southern Australia. The magnitude of the seasonal differences is particularly large in North America, the Northern Eurasian continent, and southern Australia. Furthermore, the ERA5 dataset indicates a considerably larger magnitude of σ_{DTDT} than the observations (in particular HadGHCND), primarily in the mid-to-high latitudes of the northern and southern hemispheres. This may be related to deficiencies of the HadGHCND dataset, which may have smoothed out the variability due to spatial interpolation and the lack of adequate station coverage in some regions (Fig. S1 of Wan et al. (2021)). However, σ_{DTDT} values from ERA5 are more comparable to BEST, which incorporates additional data sources beyond HadGHCND (Rohde and Hausfather, 2020).

According to equation 5, the magnitude of DTDT changes can be expressed as a function of the standard deviation σ_T, and lag-1 autocorrelation $r_{1,T}$ of daily mean temperature, which is shown in Figures 1c-f and S1e-l also show these related quantities for DJF and JJA. While observations and ERA5 mostly agree on the spatial pattern of σ_T, there is a slight overestimation of the magnitude of σ_T in ERA5 regionally during DJF (Figures 1c-d and S1e-h). This overestimation is more widespread and larger in JJA. The spatial distribution of σ_T follows a pattern consistent with σ_{DTDT}, with generally higher values in northern hemisphere mid-high latitudes ($\geq 4°C$ in DJF and 2-6°C in JJA) and southern hemisphere extratropics (2-8°C in both seasons). In comparison, the tropics exhibit smaller σ_T (1-4°C in DJF and JJA).
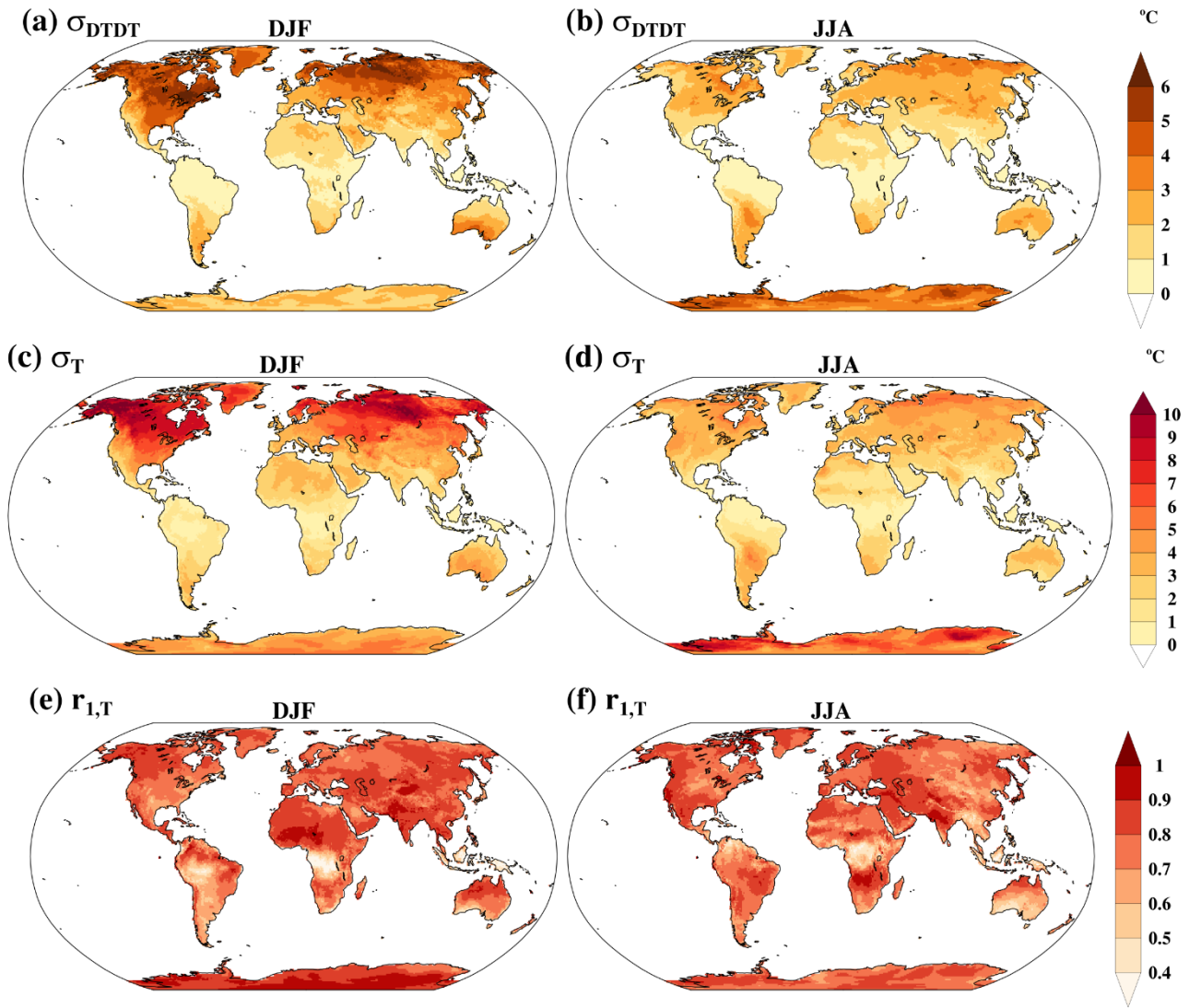
Figure 1. (a, b) Standard deviation of DTDT variations (σ_{DTDT}, °C), (c, d) standard deviation of daily mean temperature (σ_T, °C), and (e, f) lag-1 autocorrelation of daily mean temperature ($r_{1,T}$) in December-February (DJF, 1st column) and June-August (JJA, 2nd column) derived from the ERA5 dataset.

In HadGHCND, the autocorrelation is spatially rather homogeneous, while there are more pronounced spatial variations with generally lower correlations in the BEST and ERA5 datasets (Figures 1e-f and S1i-l). Autocorrelation values are typically below 0.8 (and locally below 0.6) in the deep tropics, eastern North America, the southern hemisphere land regions south of approximately 30°S, and the eastern half of the Asian continent in JJA, and above 0.8 in other regions.

Comparing the global patterns of σ_{DTDT}, σ_T, and $r_{1,T}$ shows that the spatial variation of σ_{DTDT} is mostly determined by variations in σ_T. A high standard deviation σ_T is typically associated with large σ_{DTDT} in higher latitudes, despite a relatively high $r_{1,T}$ (see again Eq. 5). At the same time, in the tropics, σ_{DTDT} is smaller because the standard deviation of daily temperature σ_T is low, even though $r_{1,T}$ is also lower. Nevertheless, $r_{1,T}$ can affect the spatial pattern of σ_{DTDT} regionally. For instance, the north-south gradient of $r_{1,T}$ over Australia in JJA leads to larger σ_{DTDT} in the south despite relatively homogeneous σ_T. With regard to the differences between observations and ERA5, both a higher σ_T and lower $r_{1,T}$ in ERA5 contribute to the typically larger σ_{DTDT} in the reanalysis data.

To gain detailed insights into the statistical distributions of DTDT changes, Figure S2 shows such distributions for selected locations around the globe—North America, Europe, South America, and Australia. In DJF, North America exhibits the highest variability of DTDT changes with a broad distribution, whereas South America shows the lowest variability with a more pronounced peak (Figure S2a). Europe and Australia experience moderate variability, intermediate kurtosis values, and a slight asymmetry (skewness) of the distribution for Australia. In JJA, South America becomes more variable, while North America, Europe, and Australia experience lower variability than in DJF (Figure S2b), consistent with the seasonal differences of σ_{DTDT} discussed above. Additionally, the distributions become more negatively skewed in JJA.

3.2 Extreme DTDT changes

To investigate extreme DTDT changes, we use the 5th and 95th percentiles as thresholds at each grid, as illustrated in Figures 2a-d. The spatial patterns of extreme DTDT changes, both warming and cooling, closely resemble those of σ_{DTDT} and σ_T, with higher values in the extratropics and lower values in the tropics (Figure 1). This similarity suggests that regions with greater DTDT variations are more prone to extreme DTDT changes. Furthermore, extreme DTDT events are more intense (i.e., exhibit a larger magnitude) during DJF than JJA, particularly in the Northern Hemisphere. In contrast, the tropics display almost equal magnitudes of extreme DTDT changes in both seasons.
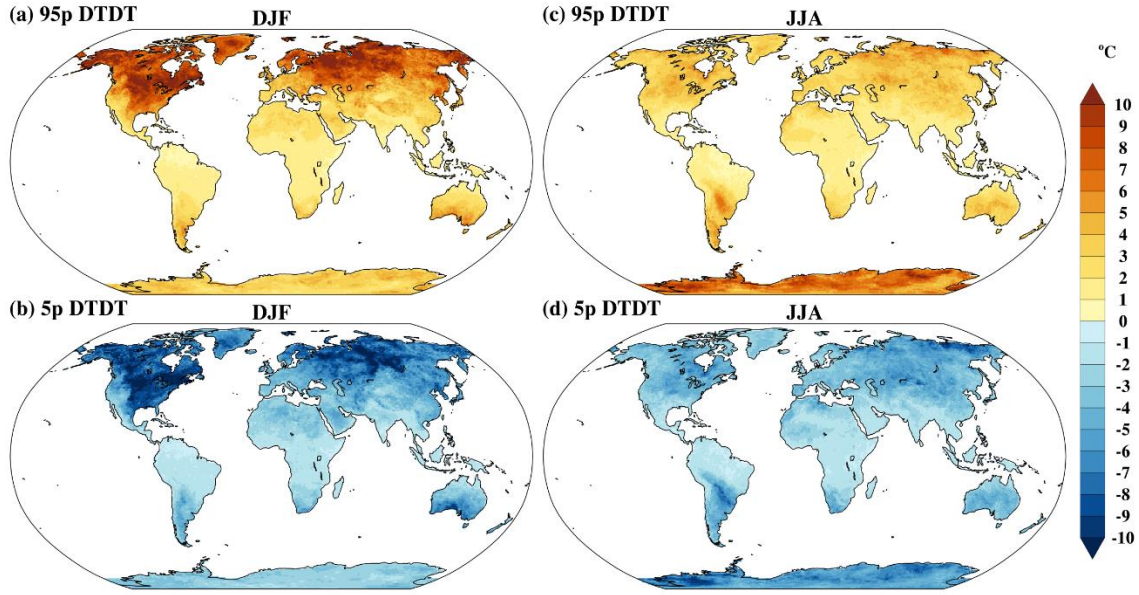
Figure 2. The (a, c) 95th percentile (95p) and (b, d) 5th percentile (5p) of DTDT changes during December-February (DJF, 1st column) and July-August (JJA, 2nd column) as derived from the ERA5 dataset.

Furthermore, to investigate how DTDT changes relate to the daily temperature of the involved consecutive days, we analyze the relationship between DTDT changes and specific quantiles (terciles) of T_t and T_{t-1}, as shown in Figure 3 for North America. Note that similar patterns are observed across other grid boxes (not shown). Our analysis reveals that extreme warming events typically originate in the lower to middle quantiles of T_{t-1} and shift toward the middle to higher quantiles of T_t. Conversely, extreme cooling events emerge from the middle to higher quantiles of T_{t-1} and transition to the middle to lower quantiles of T_t. The daily temperatures involved in extreme DTDT changes are thus not necessarily extreme but still tend to cluster in the lower/upper tails of the daily temperature distribution. The following section examines the atmospheric circulation patterns and physical processes (as described in Eq. 6) associated with extreme DTDT events at the selected global locations.
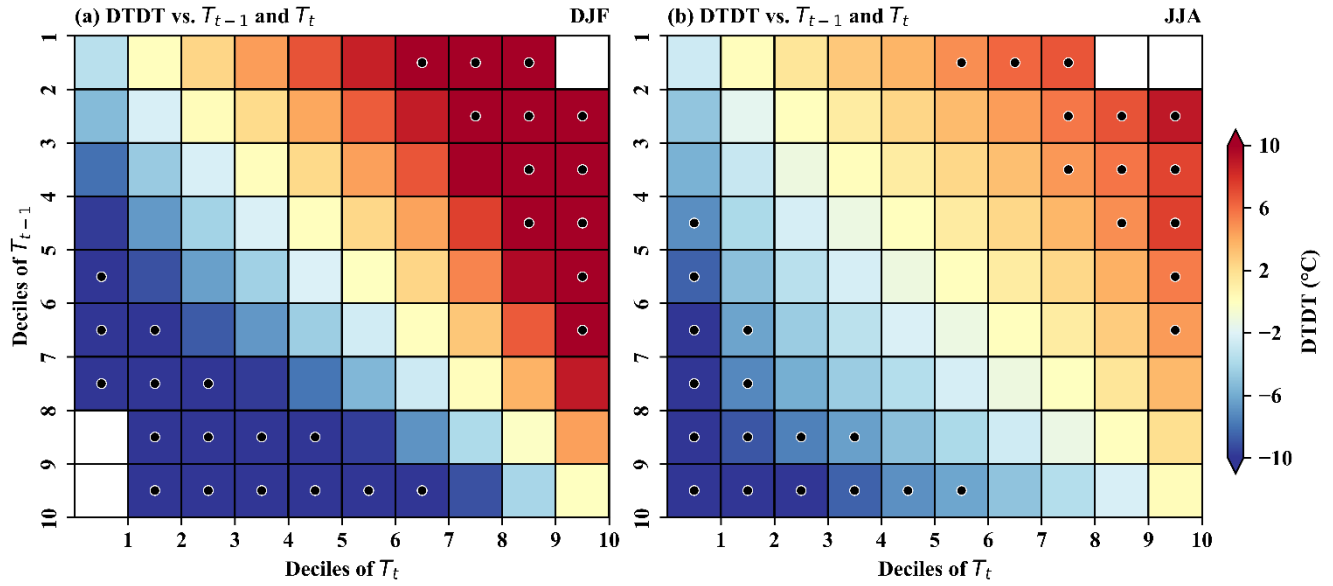
Figure 3. Heatmaps of the relationship between DTDT change and the deciles of temperature on the previous day (T_{t-1}) and the event day (T_t) for (a) December (DJF) and (b) June-August (JJA) for North America. The x-axis and y-axis represent deciles of T_t and T_{t-1}, while the color shading indicates DTDT changes, with red and blue colors indicating warming and cooling, respectively. The black circles represent extreme DTDT changes.

3.2.1 Mid-latitudes: North America

To explore the mechanism behind extreme DTDT changes in the mid-latitudes, we focus on a specific grid box in North America, which is also representative of other North American regions (compare results with Fig. S5).

The synoptic-scale circulation patterns associated with DJF warming events (exceeding the 95th percentile of DTDT changes) on consecutive days and their differences are first analyzed using composites, as shown in Figures 4a-f. On the day preceding the events (t-1), a near-surface temperature dipole is observed across northern North America, with higher temperatures in the west (≥-10°C) and lower temperatures (≤-15°C) in the east and the vicinity of the selected location (Figure 4a). This temperature pattern is influenced by a ridge over the western part, which facilitates southerly winds around its western flank, and a trough over the eastern part of the continent, associated with northerly winds (Fig. S3a). This synoptic pattern aligns with the distribution of backward trajectories, indicating the advection of cold air masses from the Arctic region (Figure 5a). Over the 3d leading up to this preceding day, these cold air masses (mean temperature of -21.5°C at -3d) experience a gradual temperature increase (of 5.7 °C), with significant adiabatic warming (8.3°C in the mean) due to a strong 100hPa mean descent (Figures 5e-f). Some diabatic cooling, likely due to longwave radiation, is indicated by a reduction in θ (by -2.6°C in the mean), constraining the temperature increase (Figure 5g). Accordingly, the temperature at t-1

is mainly determined by the advection of cold, Arctic air masses, whose temperature increases due to adiabatic warming that overcompensates a slight diabatic cooling.

240

On the days of the DJF warming events (t), the near-surface temperature reaches ≥-10°C on average, marking a notable increase compared to t-1 (Figure 4b-c). This rise is attributed to an eastward extension of the ridge, displacing the preceding trough further to the east, which leads to southwesterly wind anomalies at the selected location (Fig. S3b). The air parcel density shifts substantially southward compared to t-1, with the largest density southwest of the chosen location (40-50°N,

245   Figure 5b). This shift is associated with a substantially higher temperature 3d before arrival (-13.4°C in the mean) compared to the air parcels at t-1. The air parcels experience a vertical descent of 76hPa in the mean (Figure 5e), leading to adiabatic warming (6.7°C) and a general temperature increase in the 3d leading up to the events (Figure 5f). The net diabatic heating contribution is close to zero (0.4°C over 3d) but becomes more prominent in the last hours before the events, reaching 1.2°C in 24h (Figure 5g). Similar to t-1, the initially colder air masses are thus warmed on their way to the target location.

250   Evaluating the differences in the physical processes between the two successive days (Eq. 6) reveals that changes in advection, associated with the shift in the air mass origin and initial temperature, are the leading cause for the local DTDT warming at the selected location, contributing 8.1°C on average (Figure 5k). Reduced adiabatic warming (-1.6°C) due to a less pronounced descent on the day of the events counteracts the overall temperature increase, while reduced diabatic cooling (3°C) provides another positive contribution. This diabatic contribution is associated with the largest event-to-event variation

255   (boxes and whiskers in Figure 5k).

Warming events in JJA resemble those of DJF, including their atmospheric circulation patterns (not shown) and air parcel density distribution (Figs. S4a-b). The air parcels also experience similar adiabatic warming before arriving at the target location as in DJF, whereas the diabatic changes have a larger daily cycle and a stronger positive contribution on the last day

260   (Figs. S4e-g). The DTDT warming, as in DJF, is mainly due to the change in the air parcels' initial temperature (0.9°C at t-1 and 6.4°C at t) and thus changes in advection (Fig. S4k). Mean contributions from adiabatic warming and diabatic heating are smaller in magnitude and flip signs compared to DJF.
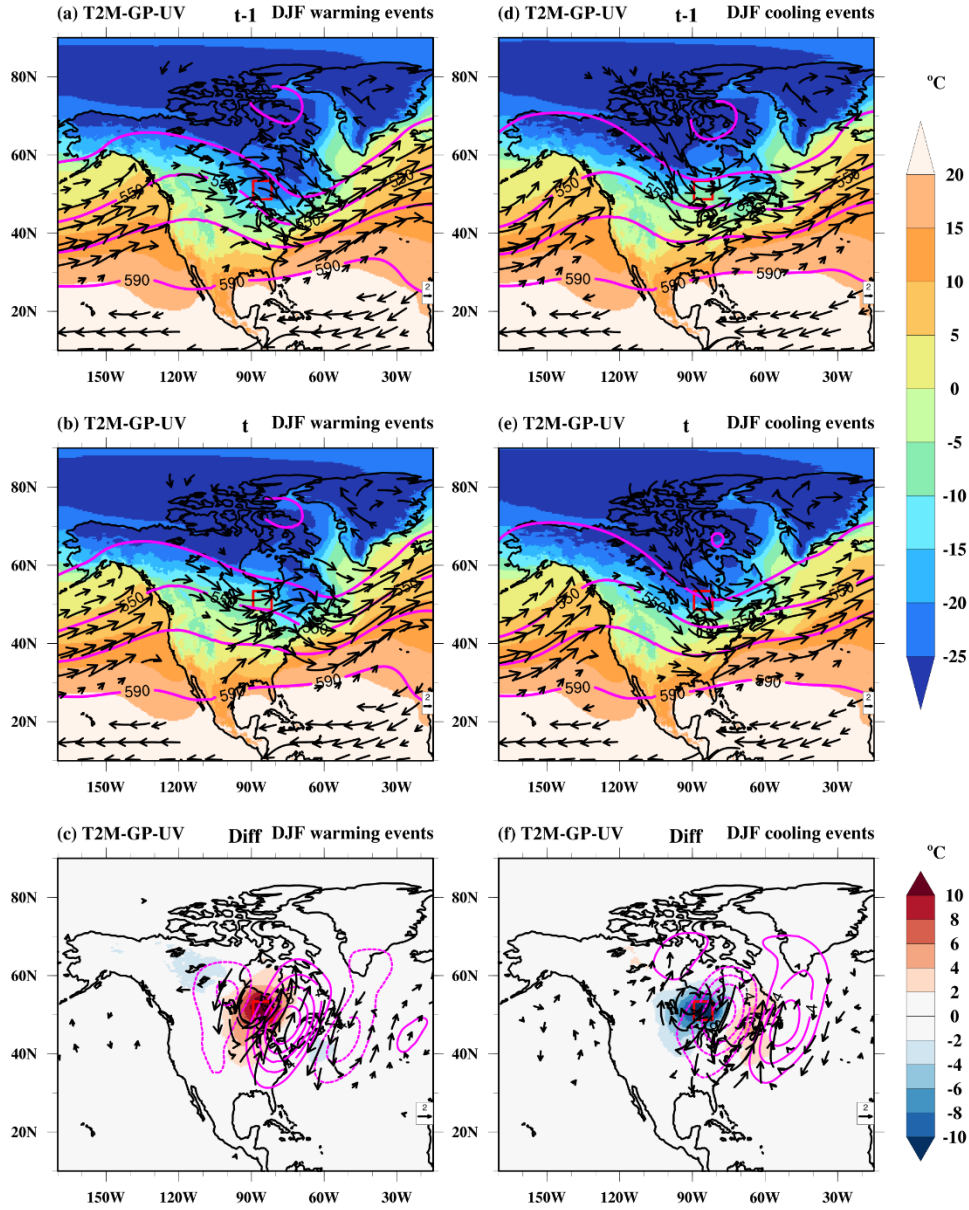
Figure 4. Composite of near-surface temperature (T2M, °C, color shading), wind at 850 hPa (UV, m/s, vectors), and geopotential
height at 500 hPa (GP, gpm, magenta contours) on the (a, d) previous day (t-1), (b, e) event day (t) and (c, f) difference (diff) of
event day and previous day of the warming (a-c) and cooling (d-f) events during December-February (DJF) at a selected grid box
in North America (red box). Note that (in a-b and d-e) wind vectors ≥5m/s and (in c, f) wind anomalies ≥1m/s are plotted. The
dotted and bold magenta contour in c and f indicates negative and positive geopotential height differences, respectively.

On the days preceding DJF cooling events (t-1), there is a pronounced meridional temperature gradient in the region of the selected location, with near-surface temperature over the northern Arctic land region below -15°C, while milder

temperatures (≥-10°C) prevail at the grid box and to its south (Figure 4d). This thermal gradient is linked to a trough over the Arctic juxtaposed with a ridge structure to its west. Southwesterly winds facilitate the transport of relatively warm air masses towards the location (Fig. S3c and Figure 5c). The transported air parcels, with a mean temperature of -15°C (at -3d), undergo a gradual descent, experiencing a modest temperature increase of about 3.7°C in 3d, attributed to the combined effects of adiabatic warming (2.4°C) and diabatic heating (1.3°C), as shown in Figures 5h-j. While the descent and adiabatic warming dominate between -3d and -2d, the last day before arrival is characterized by diabatic heating (θ increase by 2°C, Figure 5j).

On the day of the events (t), a southward shift of the Arctic trough is associated with a turn of the wind towards the north-northwest at the selected location (Figure 4e and Fig. S3d). This corresponds to the arrival of northerly air parcels with an initially extremely low temperature of -26.2°C in the mean (Figure 5d). These air parcels undergo a subsequent temperature increase of 3.2°C in 3d due to adiabatic warming (4.3°C), partly offset by radiative cooling (-1.1°C, Figures 5h-j). Accordingly, a shift to strong northerly cold advection (Figure 4f and 5d), associated with a mean temperature difference of -11.2°C between the air parcels at -3d, is the predominant contributor to the DTDT cooling events (Figure 5l). This advective effect is counteracted by moderately increased adiabatic warming (1.9°C) and complemented by amplified diabatic cooling (-2.4°C), collectively shaping the DTDT change.

In JJA, the DTDT cooling events are driven by very similar processes as the cooling events during DJF (Fig. S4). A shift from westerly to northerly transport (Figs. S4c-d) leads to a mean temperature drop of -8.6°C due to cold air advection (Figs. S4c-d and h-j). Mean changes in adiabatic and diabatic processes are very small between the two days, with larger event-to-event variation (Fig. S4l).
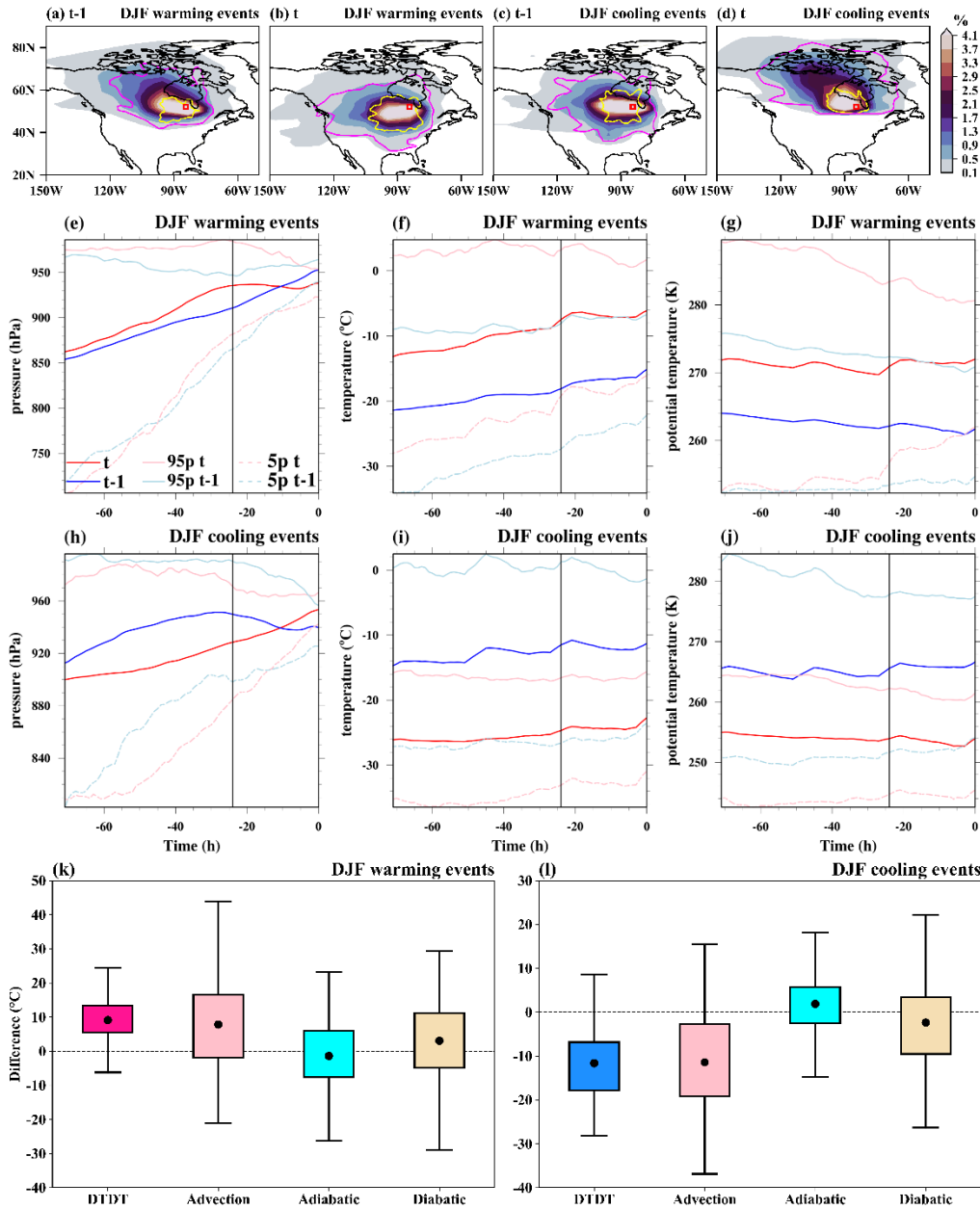
Figure 5. The spatial distribution of trajectories initiated on the previous day (t-1) and event day (t) for both December-February (DJF) warming and cooling events over North America. In the top row, the color-shading illustrates the air parcel trajectory density (%) based on the position between -5d and 0d. The magenta and yellow contours represent 0.5% particle density fields at -3d and -1d, respectively. The red box shows the selected grid box over North America. The Lagrangian evolution of distinct physical parameters (pressure, temperature, potential temperature) along the air parcel trajectories for both warming (2ndrow) and cooling events (3rd row) is presented in panels e-j. Panels k and l show the contribution of the different physical processes to the genesis of extreme DTDT changes according to Eq. (6), which refers to a 3d-time scale. The box spans the 25th and 75th percentiles of the data; the black dot inside the box gives the mean of the related quantities, and 1.5 times the interquartile range is indicated by the whiskers.

3.2.2 Mid-latitudes: Europe

Another mid-latitude location where we investigate the mechanism driving extreme DTDT variations is a grid box over Europe. This section focuses on the JJA season since the DJF events exhibit similarities with the location in North America studied in section 3.2.1.

During the preceding day of the JJA warming events (t-1), the composite geopotential height pattern features a weak trough over the eastern North Atlantic and a developing ridge over Central Europe (Figure 6a). In this situation, the northern part of Central Europe, including the selected location, is under the influence of westerlies, transporting cool, maritime air masses towards the continent (cf. Figure 7a), associated with mean temperatures below 18°C. On the contrary, Spain and western France are already affected by southwesterly winds associated with the approaching ridge, leading to higher temperatures (≥21°C) there. The mean initial temperature of the tracked air parcels 3d before arriving at the selected location is 5.4°C, and they subsequently undergo a temperature increase of about 10.1°C in 3d (Figure 7f). This increase is partly due to adiabatic warming, corresponding to a mean temperature rise of 5.7°C, which is linked to a mean pressure increase of 62 hPa. It is worth noting that this subsidence is higher between 3d and 1d before arrival and subsequently slows down when the air parcels get close to the surface (Figure 7e). Diabatic heating, likely to result from surface fluxes, increases the air temperature by 4.4°C on average, primarily on the last day before arrival.

On the day of the events (t), the trough-ridge pattern typically shifts eastward (Fig. S6b), such that Central Europe also gets under the influence of the southwesterly wind ahead of the trough (on the western flank of the ridge) and the near-surface temperature rises above 18°C (Figure 6b). This warming is associated with the arrival of air masses from western continental Europe (Figure 7b). These air parcels have a mean initial temperature of 9.3°C at -3d, which is substantially warmer than the air masses arriving at t-1, with a subsequent temperature increase of 11.4°C in 3d (Figure 7f). This warming is attributed to adiabatic warming (4.5°C in the mean, with a mean descent of 47 hPa) and strong diabatic heating (6.9°C in the mean). Comparing the contributions of processes between the two days reveals that warm air advection (3.9°C, Figure 7k) is the predominant factor driving the increase in DTDT. Further warming is facilitated by increased diabatic processes (2.5°C in the mean). Adiabatic warming, on average, has a small negative contribution (-1.2°C, the descent is larger at t-1 compared to t), albeit with a large variation between events (Figure 7k).

DJF warming events are dominated by a ridge pattern over western Europe, which weakens on the day of the events, associated with a more zonally oriented flow bringing a larger fraction of warmer maritime air masses to the selected location, which is in contrast to the mainly continental air parcel origin at t-1 (Figs. S7a-b and S8a-b). This change in origin and the associated warm advection and adiabatic warming are the leading causes of the DTDT increase, whereas diabatic cooling (-5.5K on both days) does not differ greatly between the two days (Figs. S8g and k).

335
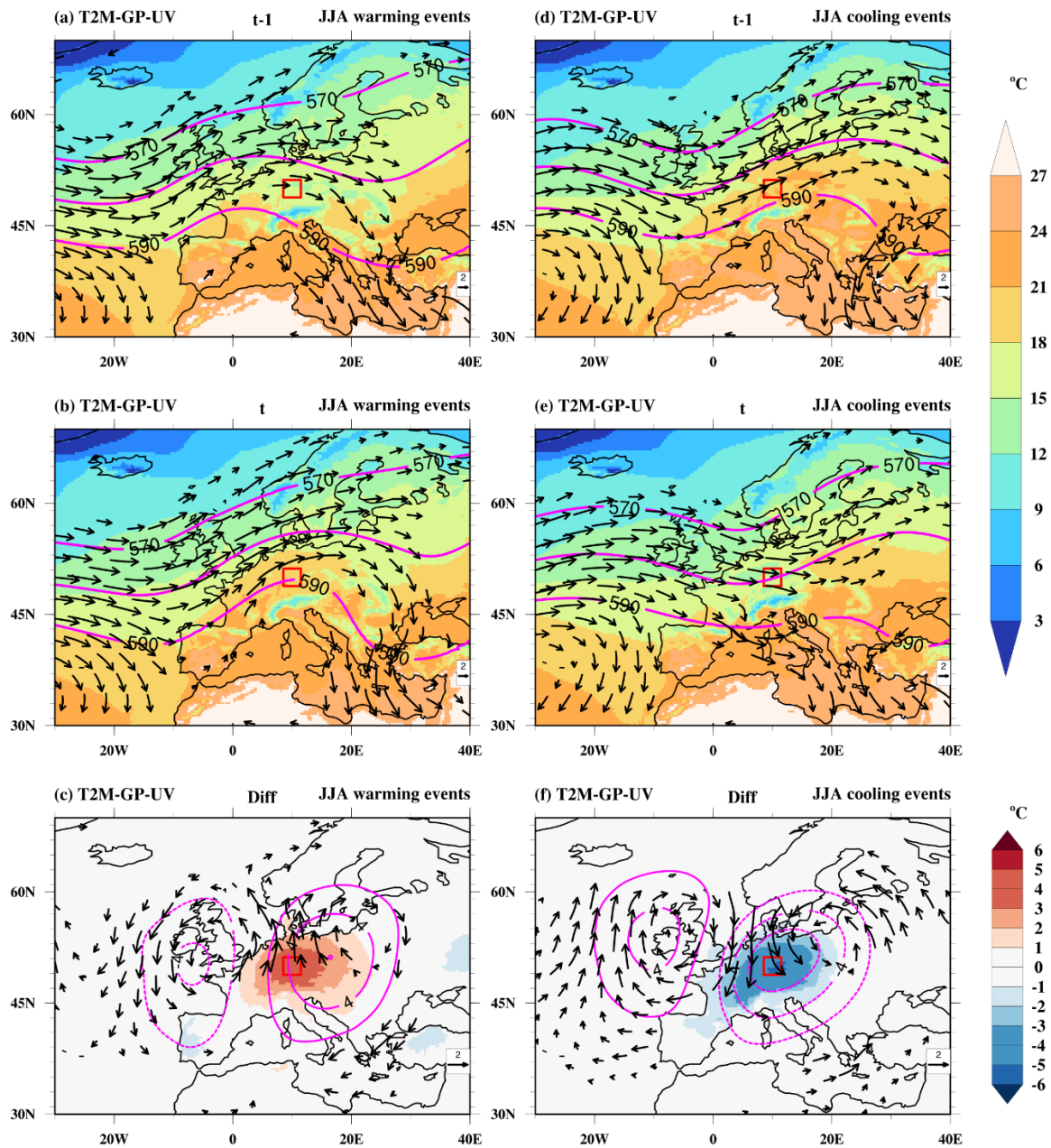
Figure 6. Composite of near-surface temperature (T2M, °C, color shading), wind at 850 hPa (UV, m/s, vectors), and geopotential height at 500 hPa (GP, gpm, magenta contours) on the (a, d) previous day (t-1), (b, e) event day (t) and (c, f) difference (diff) of event day and previous day of the warming (a-c) and cooling (d-f) events during June-August (JJA) at a selected grid box in Europe (red box). Note that (in a-b and d-e) wind vectors ≥4m/s and (in c, f) wind anomalies ≥1m/s are plotted. The dotted and bold magenta contour in c and f indicates negative and positive geopotential height differences, respectively.

During the day preceding JJA cooling events (t-1), relatively high near-surface temperatures (≥18°C) in Central Europe are associated with southwesterly winds and warm air masses linked to a trough over the British Isles and a ridge downstream over Scandinavia (Figure 6d and 7c, Fig. S6c). The air parcels are already relatively warm 3d before they arrive at the selected location (mean temperature of 13.1°C, Figure 7i) and are further heated by 5.9°C in 3d. Both adiabatic warming during their descent (3.7°C, Figures 7h-i) and diabatic heating (2.2°C, Figure 7j) contribute to this temperature increase.

On the day of the events (t), Central European temperature decreases substantially to values below 18°C, linked to a weakening of the upstream trough and eastward propagation of the ridge, leading to more zonal flow conditions (Figure 6e and Fig. S6d). Northwesterly winds carry cold, maritime air masses toward the target location, with an initial temperature of 5.4°C (Figures 7d and 7i). These air parcels are further warmed by 7.3°C due to strong adiabatic warming (5.7°C, corresponding to a mean descent of 60 hPa, Figure 7h) and some diabatic heating (1.6°C, Figure 7j) in 3d. Comparing the process contributions on the two days reveals that DTDT cooling events occur predominantly due to cold air advection by northerly winds (Figure 6f), with a mean temperature change of -7.7°C (Figure 7l). This advective effect is partly balanced by an increase in adiabatic warming (2°C). The reduced diabatic heating is small but possesses substantial event-to-event variation (Figure 7l).

DJF cooling events are triggered by a shift from westerly to northerly winds ahead of a developing ridge over the eastern North Atlantic (Figs. S7e-f and S8c-d). Air masses arriving on the day of the events have a much lower temperature at their origin (-3d) compared to the preceding day due to this northward shift in the source location (Figs. S8c-d) and a typically higher altitude (Fig. S8h-j). This leads to a pronounced contribution of advection to the DTDT decrease, which is, however, partly compensated by increased subsidence and adiabatic warming on the day of the events and a slight increase in diabatic heating (Fig. S8l).
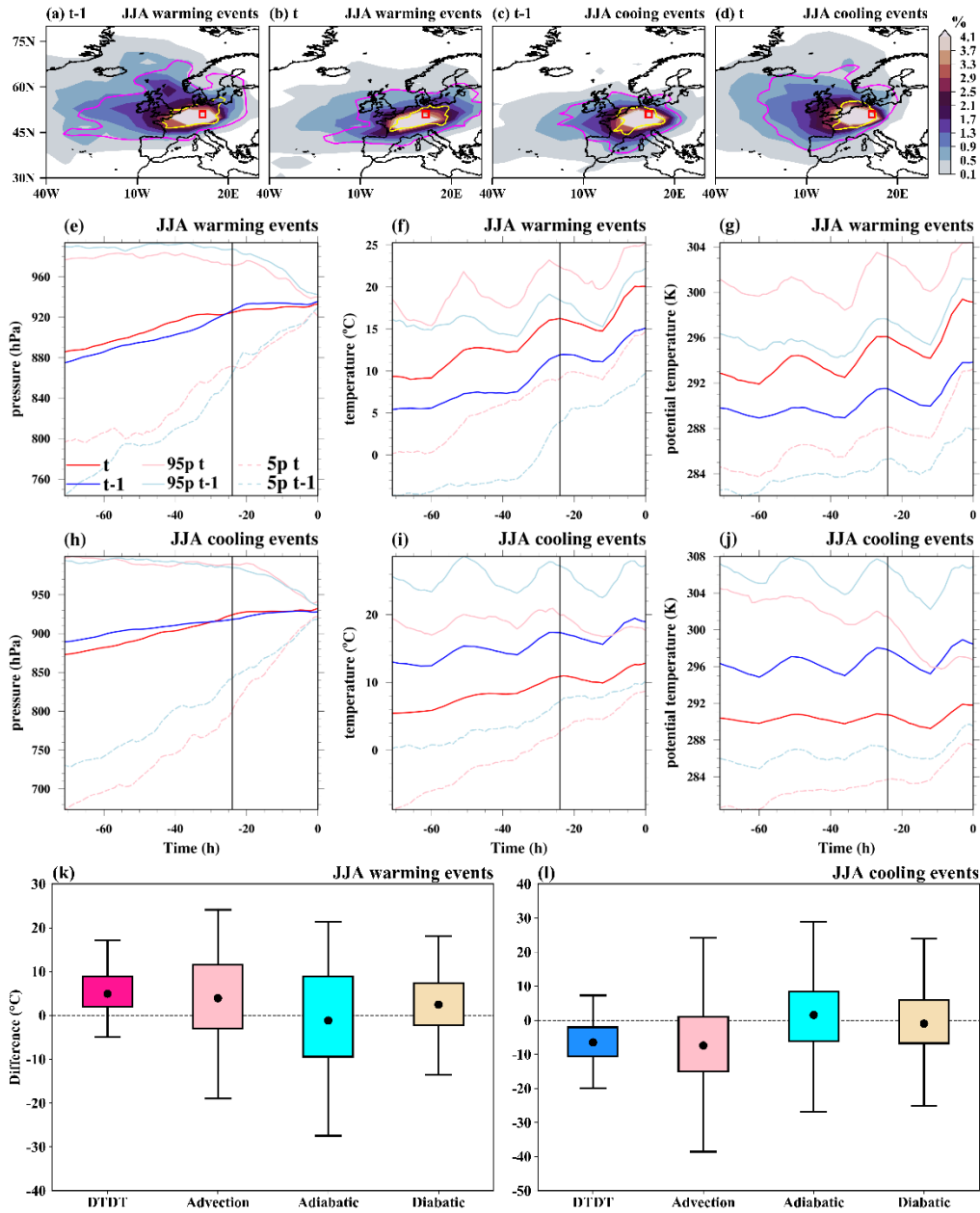
Figure 7. The spatial distribution of trajectories initiated on the previous day (t-1) and event day (t) for both June-August (JJA) warming and cooling events over Europe. In the top row, the color-shading illustrates the air parcel trajectory density (%) based on the position between -5d and 0d. The magenta and yellow contours represent 0.5% particle density fields at -3d and -1d, respectively. The red box shows the selected grid box over Europe. The Lagrangian evolution of distinct physical parameters (pressure, temperature, potential temperature) along the air parcel trajectories for both warming (2nd row) and cooling events (3rd row) is presented in panels e-j. Panels k and l show the contribution of the different physical processes to the genesis of extreme DTDT changes according to Eq. (6), which refers to a 3d-time scale. The box spans the 25th and 75th percentiles of the data; the black dot inside the box gives the mean of the related quantities, and 1.5 times the interquartile range gives the whiskers.

3.2.3 Tropics: South America

To investigate the mechanism of extreme DTDT changes in the deep tropics during DJF and JJA, we select a specific location in South America and also compare results with South Africa (Figs. S10-11), where physical processes appear to be similar.

During JJA, extreme DTDT changes over tropical South America are associated with distinct patterns, particularly in the wind field (Figs. S9a-f). On the day preceding the warming events (t-1), the selected location lies in the region of a strong horizontal temperature gradient, with higher temperatures ($\geq 22°C$) to the northeast and lower temperatures ($\leq 20°C$) to the southwest. The latter may be associated with extratropical influences, mainly through a trough over Argentina and the South Atlantic (Fig. S9a). Air parcels arriving on this day originate (at -3d) mainly from the south (Figure 8a), with a mean initial air temperature of 9.7°C that gradually increases due to adiabatic warming (4°C, descent of 41 hPa) and strong diabatic heating (9.9°C, Figures 8e-g).

On the day of the warming events (t), the trough weakens, and the winds turn easterly, which is associated with a larger fraction of air parcels originating from the east (Fig. S9b and Figure 8b). These air parcels are initially warmer (12.7°C on average) than at t-1 (Figure 8f and Fig. S9c) and again experience an average temperature increase (by 13.9°C), influenced by adiabatic warming (5.6°C, 58 hPa descent) and strong diabatic heating (8.3°C, Figures 8e-f). When examining the physical processes across consecutive days, the DTDT warming events can be attributed to a combination of factors, including warm air advection, enhanced adiabatic warming, and reduced diabatic heating (Figure 8k). Notably, all three physical factors possess substantial event-to-event variation (Figure 8l).
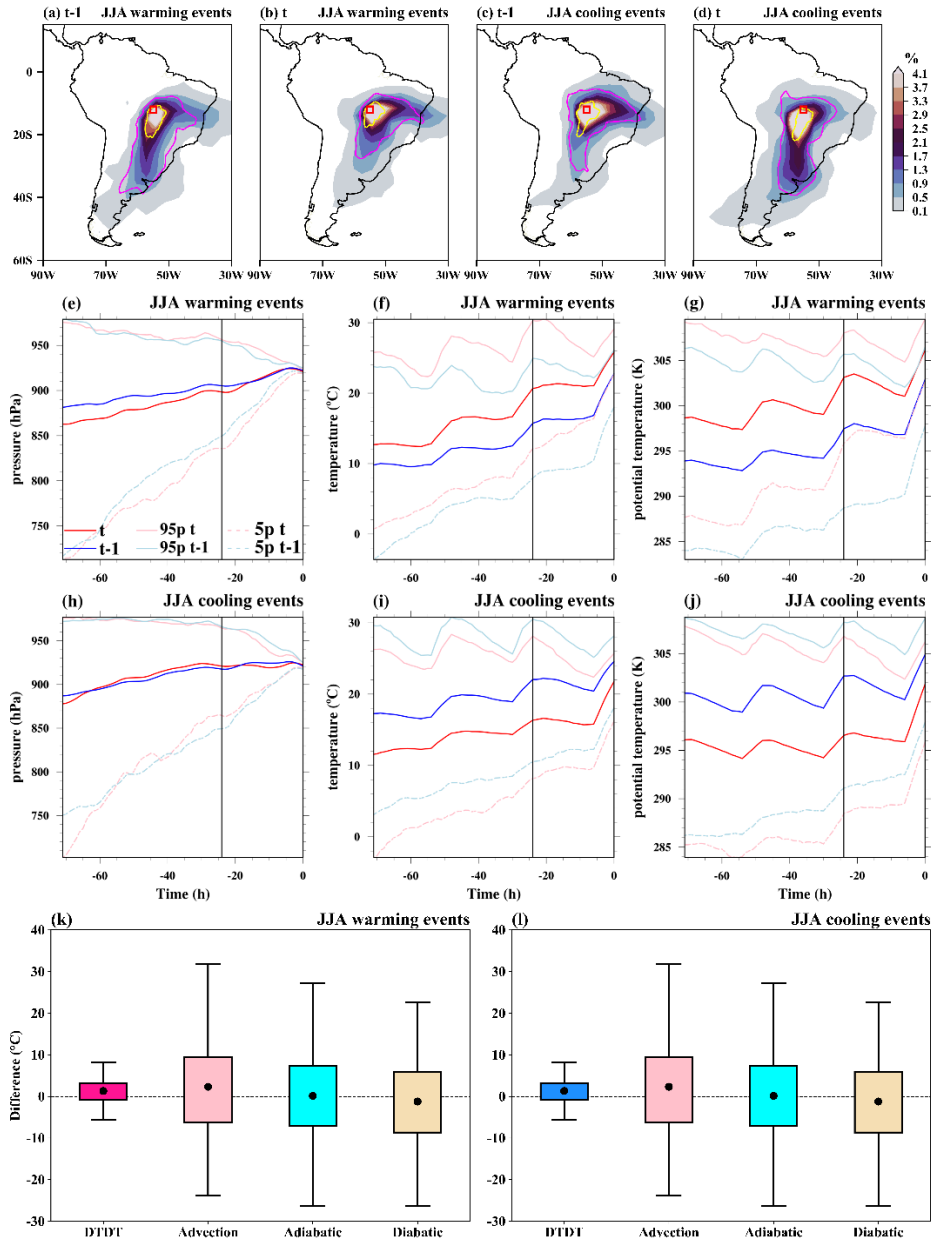
Figure 8. The spatial distribution of trajectories initiated on the previous day (t-1) and event day (t) for both June-August (JJA) warming and cooling events over South America. In the top row, the color-shading illustrates the air parcel trajectory density (%) based on the position between -5d and 0d. The magenta and yellow contours represent 0.5% particle density fields at -3d and -1d, respectively. The red box shows the selected grid box over South America. The Lagrangian evolution of distinct physical parameters (pressure, temperature, potential temperature) along the air parcel trajectories for both warming (2nd row) and cooling events (3rd row) is presented in panels e-j. Panels k and l show the contribution of the different physical processes to the genesis of extreme DTDT changes according to Eq. (6), which refers to a 3d-time scale. The box spans the 25th and 75th percentiles of the data; the black dot inside the box gives the mean of the related quantities, and 1.5 times the interquartile range gives the whiskers.

In contrast to JJA, extreme DTDT changes in DJF are not associated with clear circulation patterns. The origins of air parcels at -3d are clustered around the selected location, indicating that primarily local effects lead to the DTDT changes (Figures 9a-d). The advected temperature of air parcels on t and t-1 converge at –24h (Figure 9f), and there are only minor changes in descent and adiabatic warming between t and t-1 (Figure 9e,k). The changes are predominantly due to differences in diabatic heating on the last day before the air parcels arrive at the selected location (Figures 9e-l). To better understand these local, diabatic effects, we analyse composites of cloud cover and precipitation based on ERA5 data (Figure 10a). For DTDT warming events, high cloud coverage (90-95%), along with substantial cumulative precipitation (10-14 mm/day), is observed at t-1 across the study region, resulting in reduced diabatic heating and colder temperatures (Figures 9f-g and 10a). In contrast, cloud cover (70-75%) and precipitation (2-6mm/day) decrease on the day of the events, presumably contributing to larger diabatic heating and higher temperatures (Figures 9f, g, k, and 10b). Thus, the DTDT change during warming events is linked to a transition from primarily cloudy and wet to less cloudy and drier conditions (Figure 10c). This indicates an essential role of albedo changes and solar radiative heating in triggering the temperature increase.

The day before JJA cooling events (t-1) is characterized by high near-surface temperatures (≥24°C) at the selected location and a temperature gradient to the south (Fig. S9d). Easterly winds prevail over the study area, bringing in initially warm air parcels (17.3°C mean temperature at -3d) that undergo an additional temperature rise (7.7°C) due to adiabatic warming (3.3°C) and diabatic heating (4.4°C). In contrast, on the day of the events, colder air masses are transported to the selected location by southerly winds upstream and equatorward of a subtropical trough over south-east South America and the South Atlantic (Figure 8d and Fig. S9e), again pointing to a potential role of extratropical-tropical interactions (Fig. S9f). The air parcels originally have lower temperatures (11.4°C) than at t-1. They undergo a temperature increase (10.8°C) due to adiabatic warming (4.4°C) and diabatic heating (6.4°C, Figures 8h-j). Comparing the two days indicates that JJA cooling events are driven by cold air advection, which is partly counterbalanced by increased adiabatic warming and diabatic heating, with larger event-to-event variability (Figure 8l).
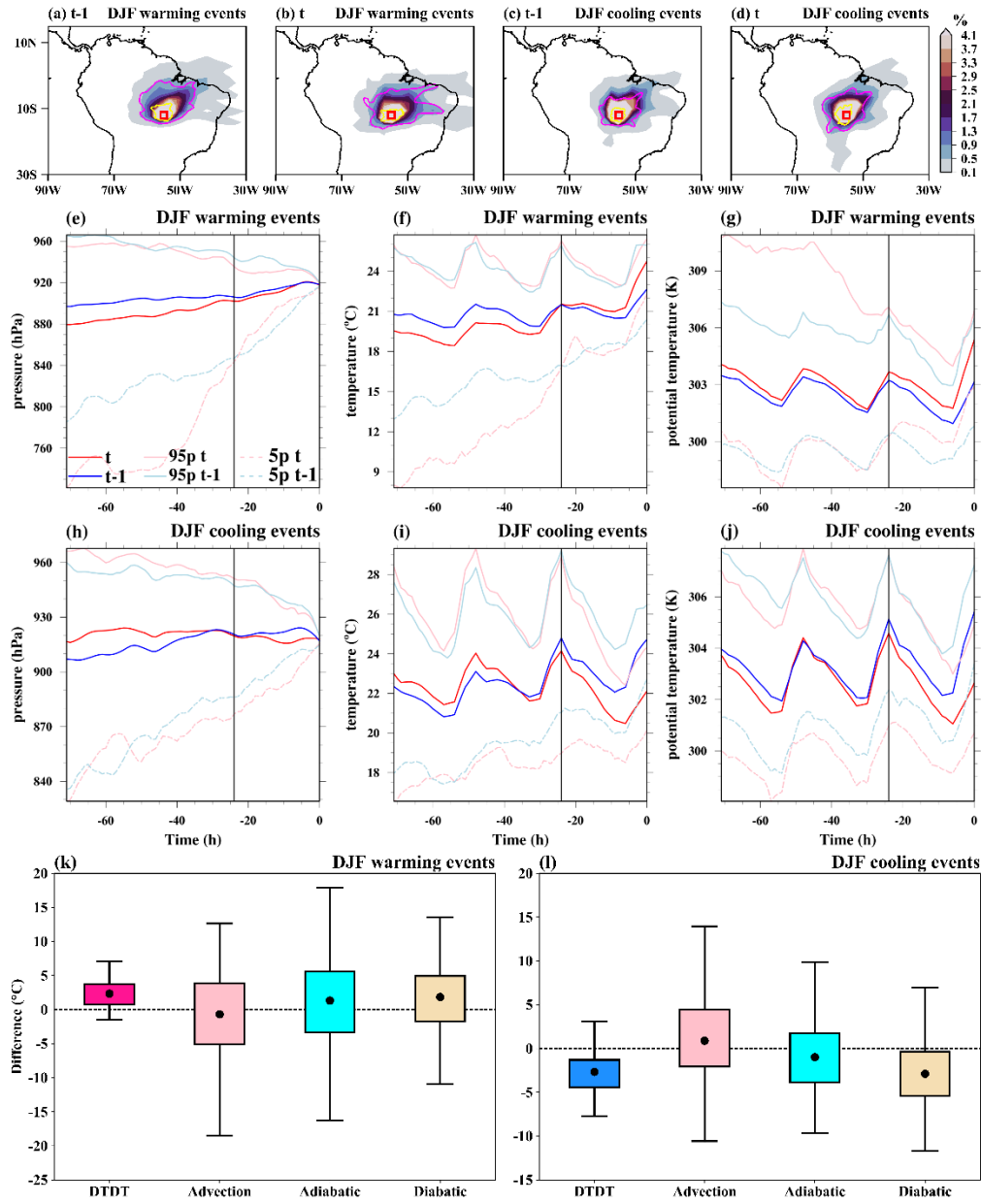
Figure 9. The spatial distribution of trajectories initiated on the previous day (t-1) and event day (t) for both December-February (DJF) warming and cooling events over South America. In the top row, the color-shading illustrates the air parcel trajectory density (%) based on the position between -5d and 0d. The magenta and yellow contours represent 0.5% particle density fields at -3d and -1d, respectively. The red box shows the selected grid box over South America. The Lagrangian evolution of distinct physical parameters (pressure, temperature, potential temperature) along the air parcel trajectories for both warming (2nd row) and cooling events (3rd row) is presented in panels e-j. Panels k and l show the contribution of the different physical processes to the genesis of extreme DTDT changes according to Eq. (6), which refers to a 3d-time scale. The box spans the 25th and 75th percentiles of the data; the black dot inside the box gives the mean of the related quantities, and 1.5 times the interquartile range gives the whiskers.

Similar to the DJF warming events, the DTDT change during DJF cooling events is primarily driven by reduced diabatic heating on the last day before the air parcels arrive at the target location (Figures 9h-j), which can be attributed to variations in local conditions. Again, like warming events, Figures 10d-f indicate that these variations are associated with changes in cloud cover and precipitation: on the preceding day, relatively lower cloud cover (70%-80%) is observed, coupled with lower total precipitation (2-8 mm/day) across the study area, ultimately resulting in higher temperatures (Figure 10d and Figure 9i). In contrast, on the day of the events, cloud cover (90-95%) and precipitation (12-20 mm/day) are higher, contributing to colder temperatures (Figure 10e and Figure 9i). Thus, DJF cooling events are linked to a transition from less cloudy and drier to cloud-covered and wet conditions (Figure 10f), again indicating a significant role of solar radiative heating (reduced diabatic heating, see Figure 9l).
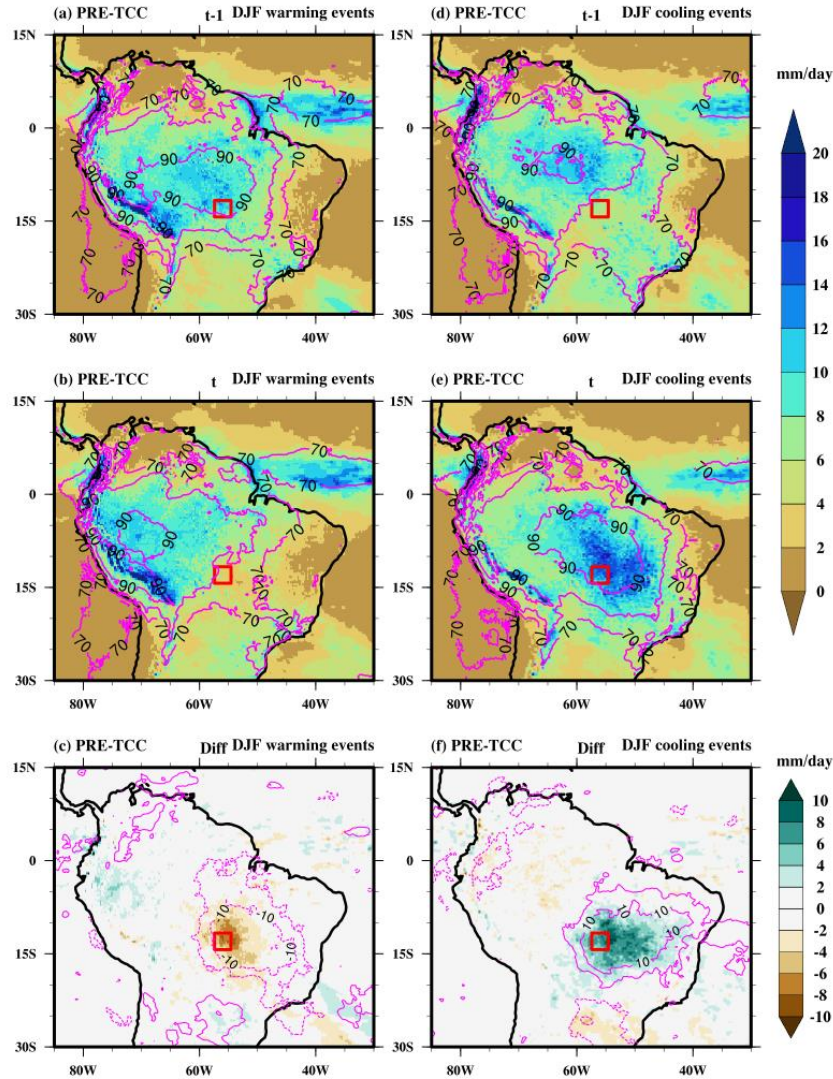
Figure 10. Composites of precipitation (PRE, mm/day, colour shading) and total cloud cover (TCC, %, magenta contours) on the (a, d) previous day (t-1), (b, e) event day and (c-f) difference (diff) of event day and previous day of the warming (a-c) and cooling (d-f) events during December-February (DJF) at a selected grid box in South America (red box). The dotted and bold magenta contour in c and f indicates negative and positive total cloud cover differences, respectively.

3.2.4 Southern Hemisphere Subtropics: Australia

We select a specific location in southern Australia to investigate the mechanism driving extreme DTDT changes over the subtropics in the southern hemisphere during DJF and JJA.

On the day preceding DJF warming events (t-1), the selected location lies in a region of weak winds in the center of a ridge and within a strong meridional temperature gradient (Fig. S12a), with higher temperatures over the continent to the north (≥24°C) and lower temperatures over the Southern Ocean (≤16°C, Figure 11a). The tracked air parcels, at -3d, are mostly located near the selected box or to its southwest (Figure 12a). Starting with relatively low temperatures (1.8°C on average),
460 they undergo substantial subsidence (147 hPa) and adiabatic warming, resulting in a noteworthy temperature increase of 13.8°C (Figures 12e-f). In addition, they experience weak diabatic heating on the day before arrival (1.8°C, Figure 12g).

The temperature increase on the day of the event is associated with intensification and eastward shift of a trough towards the Great Australian Bight and associated northerly winds (Fig. S12b), bringing warm, continental air mass to the selected
465 location (Figures 11-12b). These air parcels are slightly warmer (5.1°C) at -3d compared to t-1, also experience adiabatic warming during their descent (9.4°C, mean descent of 98 hPa), but are much more strongly affected by diabatic heating (9.9°C, Figures 12e-g). DJF warming events over the southern coast of Australia thus result from a shift from oceanic to continental air masses (Figure 11c and Fig. S12b), resulting in amplified warm air advection (3.3°C) and, more importantly, increased diabatic heating (8.1°C), most likely due to surface fluxes over the warm continent, while reduced descent and
470 adiabatic warming (-4.4°C) have a dampening effect, with substantial variability between events (Figure 12l).

The atmospheric circulation (not shown) and backward air parcel distribution during JJA warming events resemble those of DJF (Fig. S13a-b). However, most probably related to the weaker surface fluxes in Austral winter, diabatic heating does not contribute substantially to the temperature evolution along the trajectories (Fig. S13g). Consequently, the warming events are
475 primarily due to warm air advection (5.9°C), with both the adiabatic warming (- 2.2°C) and diabatic heating (- 1.4°C) terms having a damping effect (Fig. S13k).
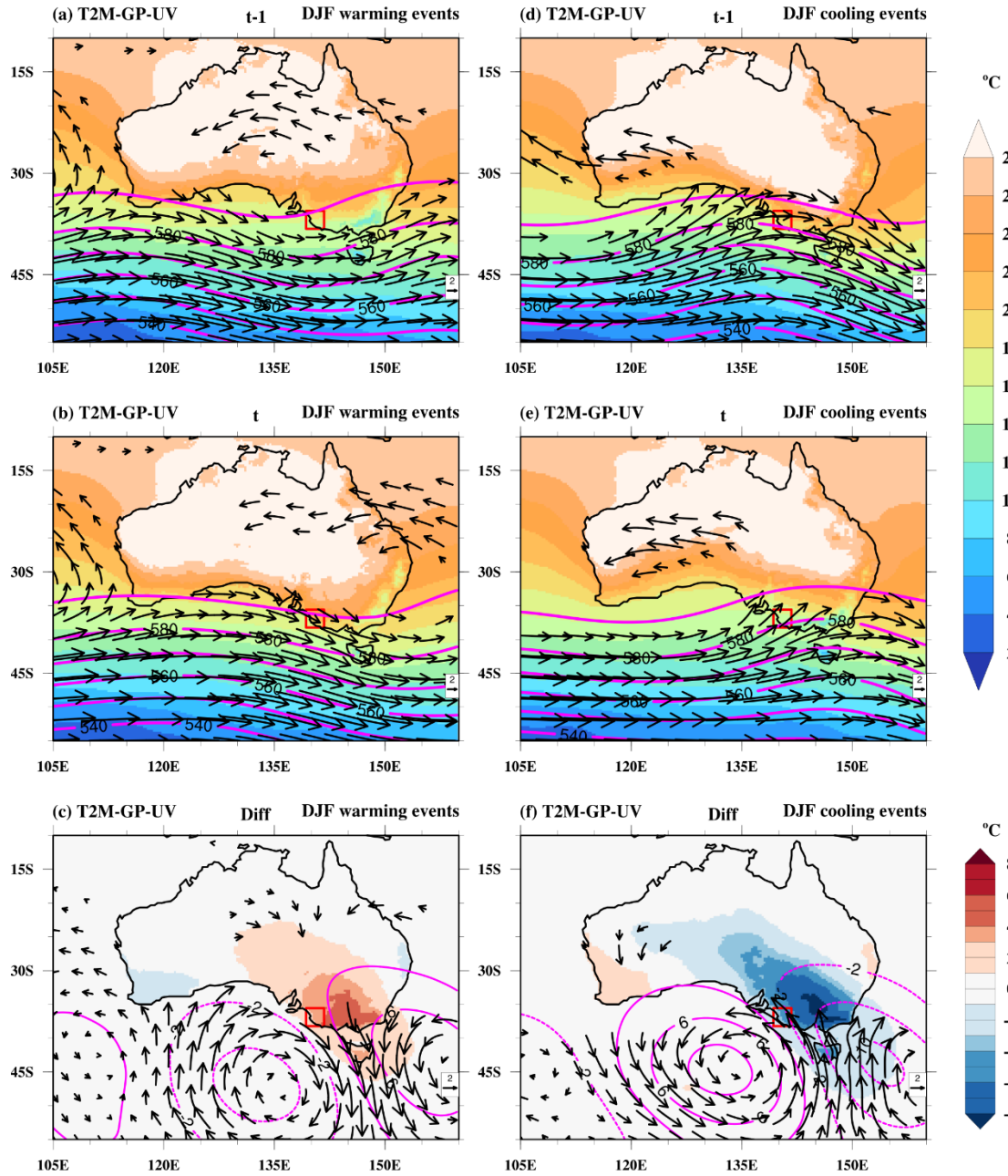
Figure 11. Composite of near-surface temperature (T2M, °C, color shading), wind at 850 hPa (UV, m/s, vectors), and geopotential height at 500 hPa (GP, gpm, magenta contours) on the (a, d) previous day (t-1), (b, e) event day (t) and (c, f) difference (diff) of event day and previous day of the warming (a-c) and cooling (d-f) events during December-February (DJF) at a selected grid box in Australia (red box). Note that (in a-b and d-e) wind vectors ≥4m/s and (in c, f) wind anomalies ≥1m/s are plotted. The dotted and bold magenta contour in c and f indicates negative and positive geopotential height differences, respectively.

480

On the day preceding DJF cooling events (t-1), a trough is located west of the selected grid box , associated with the advection of warm, continental air masses (Figures 11d, 12c, and Fig. S12c). The air particles originate at a relatively high temperature (11.2°C) and undergo subsequent adiabatic warming (8.5°C, mean descent of 89 hPa), while diabatic heating is small (Figures 12h-j). On the day of the events, the trough has moved eastward, such that the selected location gets under the influence of southwesterly wind on its western side (Figure 11e-f and Fig. S12d), leading to the advection of colder, oceanic air masses with a mean temperature of -1.8°C at -3d (Figures 12d-e). This shift to cold air advection (-13°C) is the main reason for the DTDT cooling events (Figure 12l). Adiabatic warming is very similar between the two days, while diabatic heating (2.8°C) increases slightly, dampening the temperature decrease.

Similar to DJF, JJA cooling events are characterized by a shift from continental to maritime air masses (Figs. 13c-d). The events are mainly triggered by cold air advection (-10.8°C), mitigated by increased diabatic heating (6.6°C), with adiabatic heating (1.3°C) changes being of minor importance (Fig. S13h-i and l).
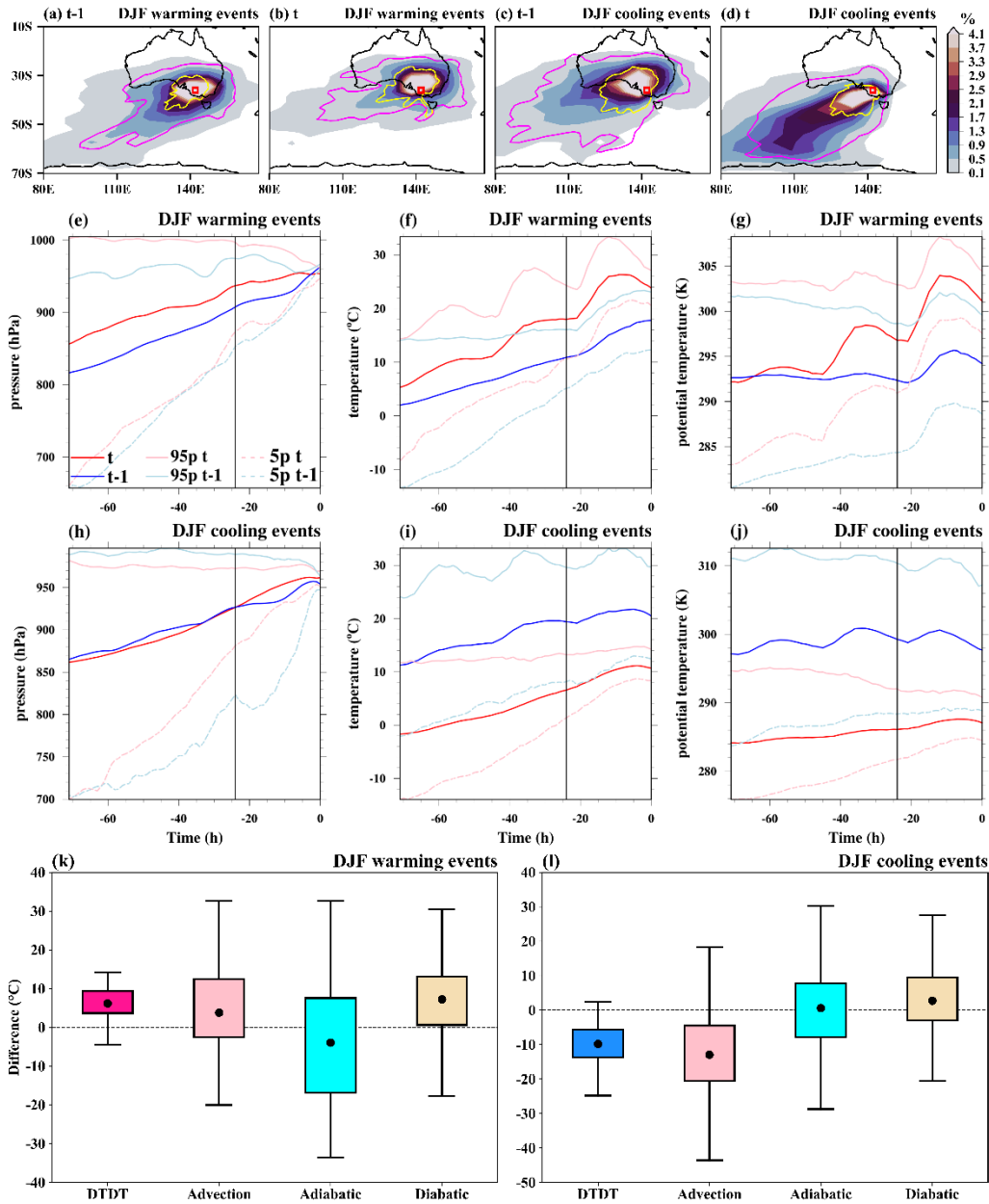
Figure 12. The spatial distribution of trajectories initiated on the previous day (t-1) and event day (t) for both December-February (DJF) warming and cooling events over Australia. In the top row, the color-shading illustrates the air parcel trajectory density (%) based on the position between -5d and 0d. The magenta and yellow contours represent 0.5% particle density fields at -3d and -1d, respectively. The red box shows the selected grid box over Australia. The Lagrangian evolution of distinct physical parameters (pressure, temperature, potential temperature) along the air parcel trajectories for both warming (2nd row) and cooling events (3rd row) is presented in panels e-j. Panels k and l show the contribution of the different physical processes to the genesis of extreme DTDT changes according to Eq. (6), which refers to a 3d-time scale. The box spans the 25th and 75th percentiles of the data; the black dot inside the box gives the mean of the related quantities, and 1.5 times the interquartile range gives the whiskers.

4. Discussion and summary

In this study, we have investigated (extreme) DTDT changes and the underlying physical processes. DTDT changes and extremes have a larger magnitude in the extratropics compared to tropical regions during both DJF and JJA, consistent with previous studies (Xu et al., 2020; Zhou et al., 2020). These spatial patterns are associated mainly with differences in the standard deviation of daily temperature, but differences in the temporal autocorrelation also play a role in some regional variations. The patterns are generally comparable between ERA5 reanalysis data and observations (particularly BEST), with typically larger magnitudes of DTDT changes in ERA5 (mostly compared to HadGHCND) due to both higher standard deviations and lower autocorrelation. The temperatures on the two days associated with extreme DTDT changes are not necessarily extreme by themselves but tend to cluster in the tails of the daily temperature distribution.

The mechanisms driving extreme DTDT changes (cooling events below the 5th percentile and warming events above the 95th percentile) have been analyzed in detail for selected locations, using a combination of Eulerian composites, and Lagrangian process analysis to decompose the effects of advection, adiabatic, and diabatic heating/cooling on a 3d-time scale. In the extratropics, extreme DTDT changes are typically associated with distinct synoptic circulation patterns, in particular troughs and ridges in the 500-hPa geopotential height field, similar to extremes of near-surface temperature (White et al., 2023; Parker et al., 2013; Nygård et al., 2023; see also Fig. S7 for a comparison). These patterns may be related to specific large-scale modes, such as the North Atlantic Oscillation, Arctic Oscillation, or Southern Annular Mode, which significantly impact air mass advection (Lee et al., 2020; Liu et al., 2023; Dai and Deng, 2021). In addition, they are likely associated with frontal passages, as explicitly shown for Europe by Piskala and Huth (2020). Future research may study such potential linkages in more detail, also at other locations.

Our trajectory analysis shows that changes in advection are the main driver of extreme DTDT changes in the extratropics, while the contributions of adiabatic and diabatic processes are generally smaller and vary more in space and also between warming and cooling events. Changes in descent and adiabatic warming between the two days of an extreme DTDT change are either small or dampen the intensity of the events, for instance, for warming and cooling events in Europe and South Asia (Figs. S15c-d) in JJA and eastern and western North America and south Asia in DJF (Figs. S5a-b and S15a-b), with the exception of warming events in eastern North America, and high-latitude North Asia (Figs. S14c-d) in JJA and Europe in DJF, where they contribute positively. Diabatic heating has a particularly strong effect on extreme DTDT changes in southern Australia, where it dampens the events' intensity in JJA but strongly amplifies warming events in the Austral summer. The latter is reminiscent of diabatic effects on wildfires and heatwaves in this region (Quinting and Reeder, 2017; Magaritz-Ronen and Raveh-Rubin, 2023). Apart from this, diabatic processes slightly amplify both warm and cold extremes in eastern North America, North Asia (Figs. S14a-b), South Asia (Figs. S15a-b), and Southern South America (Fig. 16a-b) during DJF, and primarily warming events in Europe and western North America (Figs. S5c-d) during JJA. Comparing these

processes associated with extreme DTDT changes with the mechanisms leading to usual temperature extremes (heat and cold waves) indicates similarities in the winter season when also temperature extremes are strongly affected by advection in many mid-latitude regions (Bieli et al., 2015; Nygård et al., 2023; Röthlisberger and Papritz, 2023b; Kautz et al., 2022), but larger differences in summer, when extreme DTDT events are still primarily driven by advection, whereas advection is, according to several studies, thought to play a smaller role, in particular for temperature extremes and heat waves in larger parts of the mid-latitudes (Zschenderlein et al., 2019; White et al., 2023, Röthlisberger and Papritz, 2023a).

We have studied the mechanisms associated with extreme DTDT changes in the tropics for two particular locations at 13°S in South America and South Africa (cf. Figs. S10-11) and found large differences between seasons. On the one hand, in JJA, advection is the main contributor to extreme DTDT changes, and interactions with the extratropics play a role, e.g., for the inflow of colder air masses towards lower latitudes during cooling events upstream of a subtropical trough. This configuration resembles the circulation impacting the cold waves in Central South America (Marengo et al., 2023) and South Africa (Chikoore et al., 2024) in JJA 2021. On the other hand, during DJF, extreme DTDT changes occur primarily due to local-scale diabatic processes associated with changes from cloudy conditions with precipitation to less cloudy and drier conditions or vice versa. This points to an important role of cloud radiative effects, primarily through the reflection of solar radiation, for these events (cf. (Dai et al., 1999; Betts et al., 2013; Medvigy and Beaulieu, 2012).

Our study provides the first quantitative insights into the physical atmospheric processes that lead to extreme temperature changes from one day to another. The role of changing advection from warmer or colder regions for extreme DTDT changes is apparent across all studied regions except the tropics during DJF. Such advective effects are modified by Lagrangian temperature changes due to adiabatic or diabatic processes, which tend to either amplify or dampen extremely positive (warming events) and negative (cooling events) DTDT changes, depending on the region and season. This dominant effect of advection also explains why the magnitude of DTDT changes is typically larger in the extratropics, where horizontal temperature gradients and wind velocities are larger compared to the tropics. The magnitude of the adiabatic and diabatic terms in our Lagrangian budgets is of the same magnitude in the extratropics and tropics and thus cannot compensate for this difference in advection. These mechanistic insights will be the basis for studying projected future changes in extreme DTDT changes in the second part of this study.

Appendix A

570 The DTDT (δ_T) change, as defined in Eq. (1), which has been determined based on the temperature 2m above the surface, is approximated through the average temperatures of the trajectories initiated on the corresponding day at their initiation time 0, denoted as δ_T^0:

$$\delta_T \approx \delta_T^0 = \overline{T}_t^0 - \overline{T}_{t-1}^0 \qquad\qquad (A1)$$

575 Note that the lower index here refers to the day on which the trajectories have been initiated, and the upper index refers to the time along the backward trajectory. This equation contains an approximation, as the trajectories are initialized only once a day (while δ_T refers to daily average temperatures) and from different heights above the surface, assuming (and sampling) a well-mixed near-surface layer. These trajectory temperatures can then be expressed through the Lagrangian temperature evolution:

580
$$\begin{aligned}
\delta_T^0 &= \overline{T}_t^0 - \overline{T}_{t-1}^0 \\
&= \overline{T}_t^0 - \overline{T}_t^{-3d} - \overline{T}_{t-1}^0 + \overline{T}_{t-1}^{-3d} + \overline{T}_t^{-3d} - \overline{T}_{t-1}^{-3d} \\
&= \Delta_{\overline{T},t} - \Delta_{\overline{T},t-1} + \delta_{\overline{T}}^{-3d} \qquad\qquad (A2)
\end{aligned}$$

Here, $\Delta_{\overline{T},t-1} = \overline{T}_{t-1}^0 - \overline{T}_{t-1}^{-3d}$ and $\Delta_{\overline{T},t} = \overline{T}_t^0 - \overline{T}_t^{-3d}$ denotes the Lagrangian temperature change along the trajectories on a 3-585 day timescale for the previous day and the day of the event. The term $\delta_T^{-3d} = \overline{T}_t^{-3d} - \overline{T}_{t-1}^{-3d}$ is used to measure the contribution due to advection.

This advection term differs from that of Röthlisberger and Papritz (2023b, a), who focused on daily temperature extremes and used horizontal advection of the air parcel along the climatological temperature gradient as a measure of advection in 590 their temperature anomaly budget. This is not possible here, since our diagnostic is based on absolute temperatures and not on anomalies. Technically, $\overline{T}_t^{-3d}$ represents the average temperature of the air parcels initialized on the day of the extreme event, three days before they arrive at the target location, while $\overline{T}_{t-1}^{-3d}$ represents the corresponding temperature for the air parcels initialized one day earlier. The expression in Eq. (A2), $\delta_T^{-3d} = \overline{T}_t^{-3d} - \overline{T}_{t-1}^{-3d}$ thus captures the difference in temperature between the air parcels three days before their arrival. Assuming no further temperature changes occurred during 595 transport, the DTDT change would be solely due to these initial differences. This suggests that variations in the advection of air parcels with different original temperatures between the previous day and the day of the event cause temperature changes, which is referred to as advection term here.

The Lagrangian temperature change can be further decomposed into adiabatic and diabatic contributions using the 600 thermodynamic energy Equation:

$$\frac{dT}{dt} = \frac{\kappa T \omega}{p} + \left(\frac{p}{p_0}\right)^{\kappa} \frac{d\theta}{dt} \tag{A3}$$

T is temperature, $\frac{dT}{dt}$ is the temperature change along the trajectory, $\kappa = 0.286$, p denotes pressure ($p_0 = 1000\,\text{hPa}$), ω vertical velocity in pressure coordinates, and θ the potential temperature.

Accordingly:

$$\Delta_{\bar{T},t} = \langle \int_{-3d}^{0} \frac{dT_{t,i}}{d\tau} d\tau \rangle_i \tag{A4}$$

where $T_{t,i}$ is the temperature along the ith trajectory, $\langle \ldots \rangle_i = \sum_{i=1}^{m} \frac{1}{m} \ldots \ldots$ denotes the average over the m trajectories and τ is the time along the trajectory. Inserting (A4) into (A3) yields

$$\Delta_{\bar{T},t} = \Delta_{\bar{T},t}^{adi} + \Delta_{\bar{T},t}^{dia} \tag{A5}$$

with the adiabatic term $\left(\Delta_{\bar{T},t}^{adi}\right) = \langle \int_{-3d}^{0} \frac{\kappa T \omega}{p} d\tau \rangle_i$

$$= \langle \int_{p-3d}^{p_0} \frac{\kappa T}{p} dp \rangle_i$$

and the diabatic term $\left(\Delta_{\bar{T},t}^{dia}\right) = \langle \int_{-3d}^{0} \left(\frac{p}{p_0}\right)^{\kappa} \frac{d\theta}{dt} d\tau \rangle_i$

$$= \langle \int_{\theta-3d}^{\theta_0} \left(\frac{p}{p_0}\right)^{\kappa} d\theta \rangle_i$$

Then Eq. (A2) becomes

$$\delta_T^0 = \delta_{\bar{T}}^{-3d} + \Delta_{\bar{T},t}^{adi} - \Delta_{\bar{T},t-1}^{adi} + \Delta_{\bar{T},t}^{dia} - \Delta_{\bar{T},t-1}^{dia}$$

$$= \delta_{\bar{T}}^{-3d} + \delta_{\bar{T}}^{adi} + \delta_{\bar{T}}^{dia} \tag{A6}$$

In Eq. (A6), δ_T^0 is the approximated near-surface DTDT change, $\delta_{\bar{T}}^{-3d}$ measures the mean temperature difference at the origin of the air parcels and thus the contribution of advection on a 3-day time scale, $\delta_{\bar{T}}^{adi}$ is the mean temperature difference created through adiabatic compression or expansion resulting from vertical descent or ascent, respectively, and $\delta_{\bar{T}}^{dia}$ is the contribution of mean diabatic heating or cooling from processes such as latent heating in clouds, radiation, and surface fluxes.

Code and data availability

The code of the trajectory model LAGRANTO is available at https://iacweb.ethz.ch/staff/sprenger/lagranto/download.html (Sprenger and Wernli, 2015). The HadGHCND and BEST datasets used in this study can be freely accessed from http://www.metoffice.gov.uk/hadobs/hadghcnd/download.html and http://berkeleyearth.org/data/. ERA5 data are available via the Copernicus Climate Change Service (C3S; https://doi.org/10.24381/cds.143582cf; Hersbach et al., 2018).

Author contributions

Both authors designed the study. KH performed the analysis, produced the figures, and drafted the manuscript. Both authors discussed the results and edited the manuscript.

Competing interests

Stephan Pfahl is the executive editor of WCD.

Acknowledgments

We acknowledge the HPC service of ZEDAT, Freie Universität Berlin, for providing computational Resources (Bennett et al., 2020).

References

Adams, R. E., Lee, C. C., Smith, E. T., and Sheridan, S. C.: The relationship between atmospheric circulation patterns and extreme temperature events in North America, International Journal of Climatology, 41, 92-103, 2021.

Bennett, L., Melchers, B., and Proppe, B.: Curta: a general-purpose high-performance computer at ZEDAT, Freie Universität Berlin, 2020.

Betts, A. K., Desjardins, R., and Worth, D.: Cloud radiative forcing of the diurnal cycle climate of the Canadian Prairies, Journal of Geophysical Research: Atmospheres, 118, 8935-8953, 2013.

Bieli, M., Pfahl, S., and Wernli, H.: A Lagrangian investigation of hot and cold temperature extremes in Europe, Quarterly Journal of the Royal Meteorological Society, 141, 98-108, 2015.

Böker, B., Laux, P., Olschewski, P., and Kunstmann, H.: Added value of an atmospheric circulation pattern-based statistical downscaling approach for daily precipitation distributions in complex terrain, International Journal of Climatology, 2023.

Byrne, M. P.: Amplified warming of extreme temperatures over tropical land, Nature Geoscience, 14, 837-841, 2021.

Chan, E. Y. Y., Goggins, W. B., Kim, J. J., and Griffiths, S. M.: A study of intracity variation of temperature-related mortality and socioeconomic status among the Chinese population in Hong Kong, J Epidemiol Community Health, 66, 322-327, 2012.

Chikoore, H., Mbokodo, I. L., Singo, M. V., Mohomi, T., Munyai, R. B., Havenga, H., Mahlobo, D. D., Engelbrecht, F. A., Bopape, M.-J. M., and Ndarana, T.: Dynamics of an extreme low temperature event over South Africa amid a warming climate, Weather and Climate Extremes, 44, 100668, 2024.

Dai, A. and Deng, J.: Arctic amplification weakens the variability of daily temperatures over northern middle-high latitudes, Journal of Climate, 34, 2591-2609, 2021.

Dai, A., Trenberth, K. E., and Karl, T. R.: Effects of clouds, soil moisture, precipitation, and water vapor on diurnal temperature range, Journal of Climate, 12, 2451-2473, 1999.

Dirmeyer, P. A., Sridhar Mantripragada, R. S., Gay, B. A., and Klein, D. K.: Evolution of land surface feedbacks on extreme heat: Adapting existing coupling metrics to a changing climate, Frontiers in Environmental Science, 1650, 2022.

Ghil, M. and Lucarini, V.: The physics of climate variability and climate change, Reviews of Modern Physics, 92, 035002, 2020.

Gough, W.: Theoretical considerations of day-to-day temperature variability applied to Toronto and Calgary, Canada data, Theoretical and Applied Climatology, 94, 97-105, 2008.

Hartig, K., Tziperman, E., and Loughner, C. P.: Processes contributing to North American cold air outbreaks based on air parcel trajectory analysis, Journal of Climate, 36, 931-943, 2023.

Hersbach, H.: Global reanalysis: goodbye ERA-Interim, hello ERA5, ECMWF newsletter, 159, 17, 2019.

Hersbach, H., Bell, B., Berrisford, P., Hirahara, S., Horányi, A., Muñoz-Sabater, J., Nicolas, J., Peubey, C., Radu, R., Schepers, D., Simmons, A., Soci, C., Abdalla, S., Abellan, X., Balsamo, G., Bechtold, P., Biavati, G., Bidlot, J., Bonavita, M., Chiara, G. D., Dahlgren, P., Dee, D., Diamantakis, M., Dragani, R., Flemming, J., Forbes, R., Fuentes, M., Geer, A., Haimberger, L., Healy, S., Hogan, R. J., Hólm, E., Janisková, M., Keeley, S., Laloyaux, P., Lopez, P., Lupu, C., Radnoti, G., Rosnay, P. d., Rozum, I., Vamborg, F., Villaume, S., and Thépaut, J.-N.: The ERA5 global reanalysis, Quarterly Journal of the Royal Meteorological Society, 146, 1999-2049, 10.1002/qj.3803, 2020.

Horton, D. E., Johnson, N. C., Singh, D., Swain, D. L., Rajaratnam, B., and Diffenbaugh, N. S.: Contribution of changes in atmospheric circulation patterns to extreme temperature trends, Nature, 522, 465-469, 2015.

Hovdahl, I.: The deadly effect of day-to-day temperature variation in the United States, Environmental Research Letters, 17, 104031, 2022.

Karl, T. R., Knight, R. W., and Plummer, N.: Trends in high-frequency climate variability in the twentieth century, Nature, 377, 217-220, 1995.

Kautz, L. A., Martius, O., Pfahl, S., Pinto, J. G., Ramos, A. M., Sousa, P. M., and Woollings, T.: Atmospheric blocking and weather extremes over the Euro-Atlantic sector – a review, Weather Clim. Dynam., 3, 305-336, 10.5194/wcd-3-305-2022, 2022.

Kotz, M., Wenz, L., Stechemesser, A., Kalkuhl, M., and Levermann, A.: Day-to-day temperature variability reduces economic growth, Nature Climate Change, 11, 319-325, 2021.

Krauskopf, T. and Huth, R.: Trends in intraseasonal temperature variability in Europe: Comparison of station data with gridded data and reanalyses, International Journal of Climatology, 44, 3054-3074, 2024.

Lee, D. Y., Lin, W., and Petersen, M. R.: Wintertime Arctic Oscillation and North Atlantic Oscillation and their impacts on the Northern Hemisphere climate in E3SM, Climate Dynamics, 55, 1105-1124, 2020.

Linsenmeier, M.: Temperature variability and long-run economic development, Journal of Environmental Economics and Management, 121, 102840, 2023.

Liu, G., Li, J., and Ying, T.: Atlantic multi-decadal oscillation modulates the relationship between El Niño-Southern Oscillation and fire weather in Australia, Atmospheric Chemistry and Physics Discussions, 2023, 1-17, 2023.

Magaritz-Ronen, L. and Raveh-Rubin, S.: Tracing the formation of exceptional fronts driving historical fires in Southeast Australia, npj Climate and Atmospheric Science, 6, 110, 2023.

Marengo, J., Espinoza, J., Bettolli, L., Cunha, A., Molina-Carpio, J., Skansi, M., Correa, K., Ramos, A., Salinas, R., and Sierra, J.-P.: A cold wave of winter 2021 in central South America: characteristics and impacts, Climate Dynamics, 1-23, 2023.

Matuszko, D., Twardosz, R., and Piotrowicz, K.: Relationships between cloudiness, precipitation and air temperature, Geographia Polonica, 77, 9-18, 2004.

Medvigy, D. and Beaulieu, C.: Trends in daily solar radiation and precipitation coefficients of variation since 1984, Journal of Climate, 25, 1330-1339, 2012.

Nygård, T., Papritz, L., Naakka, T., and Vihma, T.: Cold wintertime air masses over Europe: where do they come from and how do they form?, Weather and Climate Dynamics, 4, 943-961, 2023.

Parker, T. J., Berry, G. J., and Reeder, M. J.: The influence of tropical cyclones on heat waves in Southeastern Australia, Geophysical Research Letters, 40, 6264-6270, 2013.

Pfahl, S.: Characterising the relationship between weather extremes in Europe and synoptic circulation features, Natural Hazards and Earth System Sciences, 14, 1461-1475, 2014.

Pfahl, S. and Wernli, H.: Quantifying the relevance of atmospheric blocking for co-located temperature extremes in the Northern Hemisphere on (sub-) daily time scales, Geophysical Research Letters, 39, 2012.

Piskala, V. and Huth, R.: Asymmetry of day-to-day temperature changes and its causes, Theoretical and Applied Climatology, 140, 683-690, 2020.

Quinting, J. F. and Reeder, M. J.: Southeastern Australian heat waves from a trajectory viewpoint, Monthly Weather Review, 145, 4109-4125, 2017.

Rohde, R. A. and Hausfather, Z.: The Berkeley Earth land/ocean temperature record, Earth System Science Data Discussions, 2020, 1-16, 2020.

715 Röthlisberger, M. and Papritz, L.: Quantifying the physical processes leading to atmospheric hot extremes at a global scale, Nature Geoscience, 16, 210-216, 2023a.

Röthlisberger, M. and Papritz, L.: A Global Quantification of the Physical Processes Leading to Near-Surface Cold Extremes, Geophysical Research Letters, 50, e2022GL101670, 2023b.

Santos, J. A., Pfahl, S., Pinto, J. G., and Wernli, H.: Mechanisms underlying temperature extremes in Iberia: a Lagrangian 720 perspective, Tellus A: Dynamic Meteorology and Oceanography, 67, 26032, 2015.

Sarmiento, J. H.: Into the tropics: Temperature, mortality, and access to health care in Colombia, Journal of Environmental Economics and Management, 119, 102796, 2023.

Schumacher, D. L., Keune, J., Van Heerwaarden, C. C., Vilà-Guerau de Arellano, J., Teuling, A. J., and Miralles, D. G.: Amplification of mega-heatwaves through heat torrents fuelled by upwind drought, Nature Geoscience, 12, 712-717, 2019.

725 Sharma, S., Chen, Y., Zhou, X., Yang, K., Li, X., Niu, X., Hu, X., and Khadka, N.: Evaluation of GPM-Era satellite precipitation products on the southern slopes of the Central Himalayas against rain gauge data, Remote Sensing, 12, 1836, 2020.

Sheridan, S. C., Lee, C. C., and Smith, E. T.: A comparison between station observations and reanalysis data in the identification of extreme temperature events, Geophysical Research Letters, 47, e2020GL088120, 2020.

730 Sillmann, J., Croci-Maspoli, M., Kallache, M., and Katz, R. W.: Extreme cold winter temperatures in Europe under the influence of North Atlantic atmospheric blocking, Journal of Climate, 24, 5899-5913, 2011.

Simmons, A. J.: Trends in the tropospheric general circulation from 1979 to 2022, Weather and Climate Dynamics, 3, 777-809, 2022.

Sun, J. and Mahrt, L.: Relationship of surface heat flux to microscale temperature variations: Application to BOREAS, 735 Boundary-Layer Meteorology, 76, 291-301, 1995.

Wan, H., Kirchmeier-Young, M., and Zhang, X.: Human influence on daily temperature variability over land, Environmental Research Letters, 16, 094026, 2021.

Wang, F., Vavrus, S. J., Francis, J. A., and Martin, J. E.: The role of horizontal thermal advection in regulating wintertime mean and extreme temperatures over interior North America during the past and future, Climate Dynamics, 53, 6125-6144, 740 2019.

White, R. H., Anderson, S., Booth, J. F., Braich, G., Draeger, C., Fei, C., Harley, C. D., Henderson, S. B., Jakob, M., and Lau, C.-A.: The unprecedented Pacific Northwest heatwave of June 2021, Nature Communications, 14, 727, 2023.

Wu, Y., Li, S., Zhao, Q., Wen, B., Gasparrini, A., Tong, S., Overcenco, A., Urban, A., Schneider, A., and Entezari, A.: Global, regional, and national burden of mortality associated with short-term temperature variability from 2000–19: a three-stage modelling study, The Lancet Planetary Health, 6, e410-e421, 2022a.

Wu, Y., Wen, B., Li, S., Gasparrini, A., Tong, S., Overcenco, A., Urban, A., Schneider, A., Entezari, A., and Vicedo-Cabrera, A. M.: Fluctuating temperature modifies heat-mortality association around the globe, The Innovation, 3, 2022b.

Xu, Z., Huang, F., Liu, Q., and Fu, C.: Global pattern of historical and future changes in rapid temperature variability, Environmental Research Letters, 15, 124073, 2020.

Zhou, X., Wang, Q., and Yang, T.: Decreases in days with sudden day-to-day temperature change in the warming world, Global and Planetary Change, 192, 103239, 2020.

Zschenderlein, P., Fink, A. H., Pfahl, S., and Wernli, H.: Processes determining heat waves across different European climates, Quarterly Journal of the Royal Meteorological Society, 145, 2973-2989, 2019.